



## Rivers of gas - I. Unveiling the properties of high redshift filaments

Marius Ramsøy, Adrianne Slyz, Julien Devriendt, Clotilde Laigle, Yohan Dubois

### ► To cite this version:

Marius Ramsøy, Adrianne Slyz, Julien Devriendt, Clotilde Laigle, Yohan Dubois. Rivers of gas - I. Unveiling the properties of high redshift filaments. Monthly Notices of the Royal Astronomical Society, 2021, 502, pp.351-368. 10.1093/mnras/stab015 . insu-03748212

**HAL Id: insu-03748212**

**<https://insu.hal.science/insu-03748212>**

Submitted on 9 Aug 2022

**HAL** is a multi-disciplinary open access archive for the deposit and dissemination of scientific research documents, whether they are published or not. The documents may come from teaching and research institutions in France or abroad, or from public or private research centers.

L'archive ouverte pluridisciplinaire **HAL**, est destinée au dépôt et à la diffusion de documents scientifiques de niveau recherche, publiés ou non, émanant des établissements d'enseignement et de recherche français ou étrangers, des laboratoires publics ou privés.



Distributed under a Creative Commons Attribution 4.0 International License

# Rivers of gas – I. Unveiling the properties of high redshift filaments

Marius Ramsøy,<sup>1★</sup> Adrienne Slyz,<sup>1</sup> Julien Devriendt,<sup>1</sup> Clotilde Laigle<sup>1,2</sup> and Yohan Dubois<sup>2</sup>

<sup>1</sup>*Sub-department of Astrophysics, University of Oxford, Keble Road, Oxford OX1 3RH, UK*

<sup>2</sup>*Sorbonne Universités, CNRS, UMR 7095, Institut d'Astrophysique de Paris, 98 bis bd Arago, F-75014 Paris, France*

Accepted 2020 December 30. Received 2020 December 8; in original form 2020 June 24

## ABSTRACT

At high redshift, the cosmic web is widely expected to have a significant impact on the morphologies, dynamics, and star formation rates of the galaxies embedded within it, underscoring the need for a comprehensive study of the properties of such a filamentary network. With this goal in mind, we perform an analysis of high- $z$  gas and dark matter (DM) filaments around a Milky Way-like progenitor simulated with the RAMSES adaptive mesh refinement (AMR) code from cosmic scales ( $\sim 1$  Mpc) down to the virial radius of its DM halo host ( $\sim 20$  kpc at  $z = 4$ ). Radial density profiles of both gas and DM filaments are found to have the same functional form, namely a plummer-like profile modified to take into account the wall within which these filaments are embedded. Measurements of the typical filament core radius  $r_0$  from the simulation are consistent with that of isothermal cylinders in hydrostatic equilibrium. Such an analytic model also predicts a redshift evolution for the core radius of filaments in fair agreement with the measured value for DM [ $r_0 \propto (1+z)^{-3.18 \pm 0.28}$ ]. Gas filament cores grow as [ $r_0 \propto (1+z)^{-2.72 \pm 0.26}$ ]. In both gas and DM, temperature and vorticity sharply drop at the edge of filaments, providing an excellent way to constrain the outer filament radius. When feedback is included, the gas temperature and vorticity fields are strongly perturbed, hindering such a measurement in the vicinity of the galaxy. However, the core radius of the filaments as measured from the gas density field is largely unaffected by feedback; and the median central density is only reduced by about 20 per cent.

**Key words:** methods: numerical – galaxies: evolution – galaxies: formation – large-scale structure of Universe.

## 1 INTRODUCTION

Galactic surveys have revealed the presence of anisotropic structure on scales of Mpc, made up of nodes, voids, sheets, and filaments (e.g. Davis et al. 1982; de Lapparent, Geller & Huchra 1986; Geller & Huchra 1989). Cosmological simulations are able to reproduce this network, the so-called cosmic web (Bond, Kofman & Pogosyan 1996; Pogosyan et al. 1998), and unveil its existence not just for the distribution of galaxies but also for the underlying gas and DM density, as a consequence of the hierarchical growth of structures in  $\Lambda$ CDM. Gravity amplifies small anisotropies, resulting in a near homogenous background collapsing to form sheets which can collapse again along another axis to form filaments. Halos form at filament intersections where, according to cosmological hydrodynamics simulations, galaxies at high redshift grow in mass and angular momentum primarily by material transported along these filaments (Birnboim & Dekel 2003; Kereš et al. 2005; Ocvirk, Pichon & Teyssier 2008; Pichon et al. 2011; Danovich et al. 2012; Stewart et al. 2013).

While at large-scale gas filaments closely follow the structure of their DM counterparts in the cosmic web, at the scale of haloes they can penetrate deep into the virial radius and even connect to galactic discs triggering star formation episodes (see e.g. Katz et al. 2003; Kereš et al. 2005; Woods et al. 2014; Stewart et al. 2017). The erosion of these small-scale gas filaments at lower redshifts is argued to be at least partly responsible for the bimodal distribution

in colour, star formation rates, and morphology of galaxies (Dekel & Birnboim 2006) (though quenching of the largest galaxies are dependent on AGN feedback, see e.g. Croton et al. 2006). Other implicit evidence for the presence of inflows is the presence of low-metallicity G-dwarfs in the solar neighbourhood, as established in the seminal work of van den Bergh (1962). As gas depletion time-scales are estimated to be on the order of a few Gyrs for local disc galaxies (e.g. Bigiel et al. 2011; Rahman et al. 2012; Leroy et al. 2013), replenishment by inflow of pristine gas is required to match the observations. This finding is also supported by observations of extended gas discs around galaxies (co-rotating with the stellar disc), either directly in emission (e.g. from Lyman- $\alpha$ ; Prescott, Martin & Dey 2015) or indirectly in absorption (e.g. from galaxy–quasar pairs, as studied in Ho & Martin 2019; Zabl et al. 2019), all suggesting filamentary accretion from the cosmic web.

Rather than directly pursuing the filament properties themselves, it is possible to infer them through indirect methods. On large-scales, many authors have measured halo or galaxy spin alignment with cosmic filaments both in simulations (see e.g. Aragón-Calvo et al. 2007; Codis et al. 2012; Dubois et al. 2014; Laigle et al. 2015; Ganeshaiah Veena et al. 2018; Kraljic, Dave & Pichon 2019) and low- $z$  spectroscopic observations (e.g. Tempel & Libeskind 2013; Chen et al. 2019; Krolewski et al. 2019, among others). These results highlight a redshift and mass dependence of the alignment signal, with haloes with masses above  $M_h > 10^{12} M_\odot$  displaying spins perpendicularly oriented with respect to the nearest filament, whereas spins of haloes with masses below  $M_h < 10^{12} M_\odot$  align with the nearest filament. At low masses, this is thought to be due

\* E-mail: marius.ramsøy@physics.ox.ac.uk

to accretion of vorticity rich gas that drive spins to align with the filament. At high masses, this behaviour is overcome by mergers, or as Laigle et al. (2015) argues, the accretion of material from multiple vorticity domains. This dichotomy in galaxy spins shows the profound impact of cosmic filaments on the galaxies embedded within them. The inverse problem has also been studied (Pandya et al. 2019) attempting to use the alignment of galaxies to detect the cosmic web with the CANDELS survey (Grogin et al. 2011; Koekemoer et al. 2011). The non-detection of the alignment signal is likely due to the number of prolate galaxies with spectroscopically determined redshifts with stellar masses  $9 < \log(M_*/M_\odot) < 10$  in the survey, as well as these galaxies' nearest neighbours.

On smaller scales, the misalignment of gas and DM angular momenta in simulations has been attributed to different redistribution processes during halo virialization (e.g. Kimm et al. 2011; Stewart et al. 2013). However, it has also been argued that instabilities within the filaments could develop, leading to their fragmentation and breakup, thereby preventing cold gas from being smoothly accreted by the host galaxy. In such a scenario, the angular momentum segregation between DM and gas could be construed as an artefact of poor numerical resolution in filaments. Several authors (Freundlich, Jog & Combes 2014; Mandelker et al. 2016, 2019; Padnos et al. 2018; Berlok & Pfrommer 2019) carried out idealized simulations of filaments entering a halo and concluded that they should be stable, given their width and velocity. Cornuault et al. (2018) used a phenomenological model of a gas stream to explore the possibility of a turbulent, multiphase filament. The accretion efficiency of such a filament would be reduced, but it remains unclear as to whether such a multiphase model constitutes an acceptable description of cosmological filaments. Using a cosmological zoom simulation tailored to achieve maximum resolution in the filaments, Rosdahl & Blaizot (2012) find that they remain stable within haloes with masses of up to a few  $10^{11} M_\odot$  at least as low as  $z = 3$ , whilst they show more disruption within haloes of larger masses (in line with arguments made in Birnboim & Dekel 2003).

Ultimately, to distinguish between these scenarios and better assess the role played by filaments on galaxy evolution, quantitative direct measurements of their properties need to be made. However, these have proven notoriously elusive so far (see e.g. Kimm et al. 2011, for a more detailed discussion). Indeed, direct observations of the distant cosmic web suffer from the steep scaling of surface brightness with redshift, which makes the cold filaments extremely hard to detect in emission (though not impossible, see e.g. Giavalisco et al. 2011; Ribado et al. 2011; Kacprzak, Churchill & Nielsen 2012; Martin et al. 2016; Gallego et al. 2018; Elias et al. 2020), and thus rely on stacking or back-lighting by a bright source. Future surveys using the *James Webb Space Telescope* (JWST; Gardner et al. 2006) while being insensitive to the smoothly accreting gas itself, the telescope will be sensitive to a range of associated phenomena. Filaments are typically traced by Lyman- $\alpha$  blobs (LABs) and emitters (LAEs; e.g. Kikuta et al. 2019; Umehata et al. 2019), which will be observable by the NIRSpec instrument (Latif et al. 2011). In addition, LAEs should be detectable with the proposed BlueMUSE instrument. On larger scales, filamentary gas can be detected in the radio with the Square Kilometer Array (Kooistra et al. 2019). Lyman- $\alpha$  forest tomography also allows the probing of the cosmic web in the IGM, with the feasibility of observations for the Very Large Telescope investigated by (Lee et al. 2014) and the European Extremely Large Telescope by (Japelj et al. 2019). This will enable the detection and exploration of the full three-dimensional structure of the cosmic web.

Efforts to understand observed filament properties are correspondingly mirrored by simulations (e.g. Gheller et al. 2015, 2016). On

large scales, filaments of the cosmic web are reported to have a radial power-law profile in density with a power-law index comprised between  $-1$  and  $-2$  (see e.g. Colberg, Krughoff & Connolly 2005; Dolag et al. 2006; Aragón-Calvo, van de Weygaert & Jones 2010). Smaller scale studies have been performed by e.g. Ocvirk et al. (2016), who determined the outer radii of filaments in their simulation to be about  $50 h^{-1} \text{ kpc}$  at  $z = 4.3$  by looking at the separation between temperature peaks caused by the accretion shock, although these authors acknowledge that they did not separate edge-on sheets from filaments in their sample. Using cosmological simulations, Dekel et al. (2009) found that DM filament radii are comparable to the virial radius of the haloes they connect, and that the cold gas streams residing within the haloes are considerably narrower, typically a few percent of the virial radius.

The scale-free nature of CDM results in progressively smaller filaments feeding into larger ones at all scales, down to the numerical resolution of the simulation in this case. However, alternative DM theories could result in different DM structures, (e.g. Warm DM Gao & Theuns 2007). This produces filaments down to Mpc-scales, while erasing smaller scale structure. Mocz et al. (2019) studied filaments under the Fuzzy DM regime, where an additional quantum pressure prevents the formation of lower mass filaments. Both WDM and FDM result in higher density filaments at earlier times, with the formation of population III occurring within them (Mocz et al. 2019), further distinguishing these versions of DM from CDM. It is possible that the supernovae of these stars will be detectable with JWST (Hartwig, Bromm & Loeb 2018).

To date, the rich complexity of the filamentary network connecting haloes of various masses and its evolution with redshift has yet to be investigated systematically. In this paper, we argue that to do so, it is pivotal to work on a cosmological sample of *well-resolved* filaments and take a step in this direction by measuring filament profiles from the density, vorticity, and temperature field information available in a zoom-in cosmological simulation. Our focus is on intermediate-scale filaments, that is, those connecting to a  $M_*$  galaxy, at moderate to high redshift ( $z \geq 3$ ). We also investigate how stellar feedback can perturb these filaments. Given the limited sample considered in this work, it should be considered a pilot study. In an upcoming paper, the methods developed here will be applied to New-Horizon, a larger volume simulation [ $\sim 4200 (\text{Mpc}/h)^3$ ] with similar resolution (Park et al. 2019; Dubois et al. 2020), where a statistical sample of filaments can be obtained, connecting a more diverse ensemble of galaxies.

The structure of this paper is as follows: In Section 2.1, we outline the simulation set up. In Section 2.2, we describe how we identify the filaments and perform the analysis. Section 3 presents the results of our work, compares filament properties to an analytic model and discusses the robustness of our measurements vis-à-vis resolution. We summarize our results in Section 4.

## 2 NUMERICAL METHODS

### 2.1 Simulations

The analysis is performed on two simulations of the NUT suite (Powell, Slyz & Devriendt 2011), a series of cosmological zoom-in simulations of a Milky-Way-like galaxy designed to study the effects of resolution and various physical processes on its formation and evolution using the Adaptive Mesh Refinement (AMR) code RAMSES (Teyssier 2002). Initial conditions are generated at redshift  $z = 499$  using the MPGratic code (Prunet et al. 2008) with cosmological parameters set in accordance with the WMAP5 results (Dunkley et al. 2009). The simulation volume is a cubic box  $9 h^{-1} \text{ Mpc}$  on a side and

a coarse root grid of  $128^3$  cells. A series of three nested grids are then centred on a sphere with radius  $2.7 h^{-1}$  Mpc which encompasses the Lagrangian volume occupied by the galaxy (host DM halo mass of  $M_{\text{vir}} = 5 \times 10^{11} M_{\odot}$  by  $z = 0$ ). AMR refinement is then enabled within that sphere using a quasi-Lagrangian refinement criterion to achieve a maximal spatial resolution of 10 pc at all times whilst forcing the mass of each individual cell to remain roughly constant. The collisionless fluid in this high resolution region consists of dark matter (DM) particles each with mass  $5.6 \times 10^4 M_{\odot}$ , whereas the gas evolution equations are solved on the AMR grid by means of a Godunov method (HLLC Riemann solver) with a MinMod limiter to reconstruct variables at cell interfaces. The gas density field in the simulation is shown in Fig. 1 at  $z = 4$ , gradually zooming in from the full box on to the central galaxy itself.

In this paper, we use a NUT simulation with no feedback, and one with mechanical supernova feedback as defined in Kimm et al. (2015). In the following, we refer to these two simulations as the ‘no-feedback’ and ‘feedback’ runs, respectively. The feedback recipe of Kimm et al. (2015) ensures that the appropriate energy or momentum is deposited into the cells around the supernova, depending on whether the Sedov–Taylor phase of the blast wave is resolved or not. This prevents the supernova energy from being artificially radiated away, as would happen if solely thermal energy was injected (the so-called overcooling problem described in Katz 1992). Both runs under study use cooling tables calculated by Sutherland & Dopita (1993), down to  $10^4$  K, and the Rosen & Bregman (1995) approximation for temperatures below this threshold. A UV background is instantaneously turned on at  $z = 8.5$  to account for the re-ionization of the Universe, while star formation is allowed to proceed when gas densities become greater than  $4 \times 10^2 \text{ H.cm}^{-3}$  with an efficiency of 1 per cent per free-fall time, calibrated on observations by Kennicutt (1998). A detailed description of the implementation of star formation used in this version of RAMSES may be found in Rasera & Teyssier (2006) and Dubois & Teyssier (2008). For the feedback run, a Chabrier initial mass function (Chabrier 2003) is adopted, with 31.7 per cent of the mass fraction of each star particle ending up as a single type II supernovae and releasing  $10^{50} \text{ erg } M_{\odot}^{-1}$  of energy after a 10 Myr time delay and expelling heavy elements with a 5 per cent yield.

## 2.2 Filament Identification

As we aim to measure the properties of the cosmic web filaments, both in the DM and gas density fields, we now describe how we identify these structures in the simulations.

### 2.2.1 Method

The DM particle distribution is tessellated using the Delaunay Tessellation Field Estimator tool (Schaap 2007) and fed to the code DISPERSE (Sousbie 2011). DISPERSE computes stationary points (maxima, minima, and saddle points) of the density field using the Hessian matrix and assigns to each pair of critical points (e.g. maxima–saddle) a persistence, namely a measure of how significant it is with respect to a Poisson distribution. The persistence threshold is the single parameter that determines which features are considered as noise and which robustly pertain to the topology of the underlying density field. From this set of stationary points that characterize the topology of the field, DISPERSE connects saddles to maxima following the direction of least gradient to create a network of filaments which

will be referred to in this paper as the ‘skeleton’, and we will call ‘nodes’ the maxima of the density field.

### 2.2.2 Extraction of the skeleton from the simulations

For each simulation, filaments are extracted from the Delaunay tessellation reconstruction of the DM density field, setting a persistence threshold of  $10\sigma$ . This persistence threshold is chosen such that the observed skeleton is in good visual agreement with the DM density field. Our results are in fact insensitive to the exact value chosen for this threshold, as we are only studying the main filaments feeding the galaxy (see Section 2.2.3). The skeleton is additionally processed with SKELCONV (see DISPERSE manual<sup>1</sup>) using the BREAKDOWN and SMOOTH functions. BREAKDOWN removes duplicate segments entering a node from two different starting points. These segments can be so close as to be indistinguishable from one another and as such are removed to prevent their overrepresentation in the final skeleton. The skeleton is then smoothed by averaging over the positions of the 30 nearest neighbours of each segment. This mitigates the effects of Poisson noise on the skeleton, ensuring that individual segments locally follow the global direction of the filament they belong to.

In both the feedback and no-feedback runs, 1.22 physical kpc is the maximum spatial resolution reached in filaments, defined as the size of an individual cell on the highest AMR grid level that entirely maps the filament (see Fig. 2). As is clear from Fig. 2, higher refinement levels are triggered within filaments but their coverage is patchy, and mostly concentrated around haloes/galaxies embedded within these elongated structures. As we argue in our convergence analysis (Section 3), we believe 1.22 kpc is enough to resolve the radial structure of filaments, at least those that connect to haloes/galaxies with masses similar (or larger) to the one that we study in this paper (roughly  $M_*$ ). We emphasize that this is a much higher resolution than that currently reached in large-scale cosmological hydrodynamics simulations, where  $\simeq 1$  kpc resolution is only attained within galaxies (e.g. Dubois et al. 2014; Vogelsberger et al. 2014; Schaye et al. 2015; Nelson et al. 2018, 2019; Davé et al. 2019). The main drawback of our study is that such resolution is obtained at the cost of simulating a much smaller volume, and thus, focuses on a single object. Filament extraction is performed at the maximum level of resolution thus defined. However, as highlighted by Rosdahl & Blaizot (2012) and in our convergence study (Section 3), increasing the resolution does not seem to affect the filament properties much, and we, thus, expect that our results only weakly depend on resolution.

Finally, we note that DISPERSE applied to the DM particle distribution, as is done in this paper, only allows the extraction of the filaments down to a scale comparable with the virial radius of DM haloes. Below this scale, DM filaments (at least in standard 3D space) are washed out by the virialization process at the origin of halo formation and evolution. Therefore, we restrict our measurements of filament properties to filament segments located outside of the virial radii of embedded DM haloes.

### 2.2.3 Identifying the main filament

The gas and DM distributions differ significantly even for the no-feedback run (compare left-hand and middle panels of Fig. 3), with the gas density field presenting much fewer filamentary structures

<sup>1</sup><http://www2.iap.fr/users/sousbie/web/html/index4f3e.html?category/Manual>



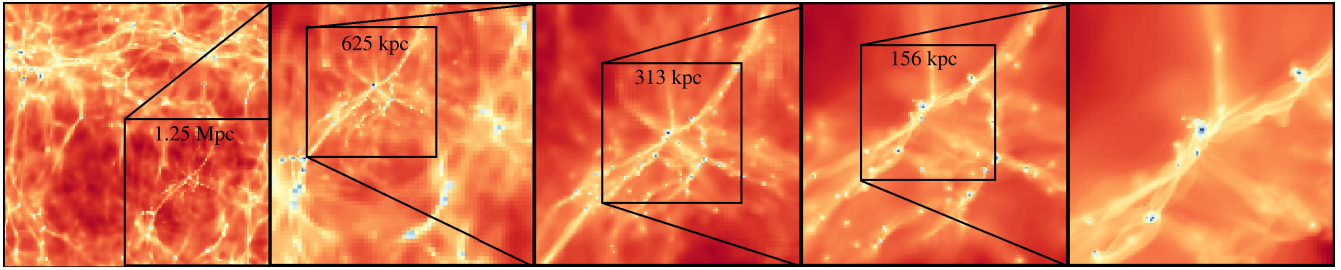


**Figure 1.** Zooming in on the NUT galaxy gas density field at  $z = 4$ . The leftmost panel shows a gas density projection of the entire simulation volume (12.5 comoving Mpc), with the high resolution zoom region enclosed in the square located in the bottom right-hand corner of the first panel. Each subsequent panel, going from left- to right-hand panel, displays a projection of 1/8th of the volume of the previous panel. The size of each volume in physical units is indicated. The middle panel shows the region within which the analysis in this paper is performed, chosen so as to maximize the length of the studied filament.

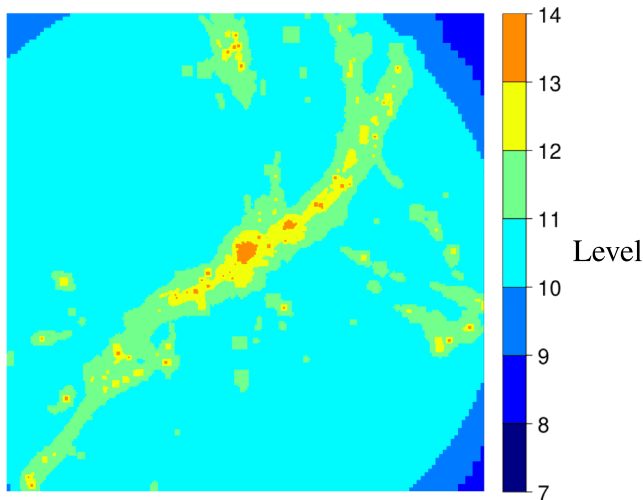


**Figure 2.** Resolution map for a slice of thickness 300 pc, across a  $(625 \text{ kpc})^2$  region of the computational domain at  $z = 4$ , with each colour representing a different resolution level as indicated on the figure. At this redshift, the filament is uniformly sampled at 1.2 kpc resolution (AMR level 11: green) and partly at 0.61 kpc (AMR level 12: yellow) around the most massive haloes embedded in it. Even though the highest spatial resolution reached in the simulation is 10 pc, which corresponds to AMR level 20, levels above 13 are not shown as they are confined to the galaxies themselves and their immediate vicinity.

than the DM.<sup>2</sup> In addition, even though dwarf galaxies residing within filaments are affected by feedback, the impact of this feedback on the growth of the central galaxy is minimal (it does not lead to the disruption of the main filament) as the majority of the gas feeding it at high redshift is accreted via filaments, and not from mergers (Danovich et al. 2012; Tillson et al. 2015). However, the gas density field in the run with feedback will be more perturbed due to interactions with galaxy winds and shocks (see middle and right-hand panels of Fig. 3), making the comparison between feedback and no-feedback runs difficult. Furthermore, DISPERSE is designed to work with particle data, as it allows in this case a meaningful definition of persistence (the very concept of which relies on quantifying the significance of a feature with respect to Poisson noise). For these reasons, and given that we are not interested in probing the existence

<sup>2</sup>This is a consequence of re-ionization reheating the gas of the IGM and preventing accretion into the shallow potentials of DM filaments (Katz et al. 2019).

of filaments within the virial radius of DM haloes in this work, the DM density field seems more appropriate to carry out filament extraction.

We therefore elect to extract the skeleton from the DM density field, but trim it in order to keep only the main filament, along which most material flows on to the galaxy. For an  $M_*$  central galaxy, the main filament traced in the gas clearly coincides with its DM counterpart (see top panels of Fig. 3). As we are analyzing a filament connecting to a single object, we identify the approximate region where it begins and ends by eye, and select the highest density point in this region as its starting/end point.<sup>3</sup> We then use Dijkstra's algorithm (Dijkstra 1959) to compute the shortest path (following the skeleton) between the start and end points. This works by assigning to each segment a distance from the start point, travelling along all the various possible paths of the skeleton. Whenever a shorter path to a given segment,  $s$ , is found, then the selected path is updated up to  $s$ , and the distances to all segments connected to  $s$  along this path which have a longer path-length, are updated. This process is iterated until the network is traversed, yielding the shortest path between the given start and end point. The method is valid provided the main filament flows mostly straight on to the galaxy, which, in turn, holds until the filament gets close to the galaxy disc (Powell et al. 2011).

In order to avoid the filament passing through haloes, filament segments located in regions with densities higher than 130 times the mean density of the Universe were excluded.<sup>4</sup> This density threshold is chosen empirically, but the resulting skeleton does not depend very sensitively on the chosen value provided this latter is on the order of 100 times the mean density of the Universe. The entire initial filamentary network and the resulting main filament extracted after post-processing are shown in Fig. 4. Fig. 3 highlights that the skeletons extracted from the DM density fields of the feedback and no-feedback runs are slightly different. In this figure, one can clearly see a pair of filaments on the left-hand side of the central galaxy, which are in the final stages of merging. As a result, our algorithm identifies two possible paths along which the main filament would have essentially the same length. Small changes in the noise level associated with the DM particles in the two different runs change the

<sup>3</sup>For larger volume cosmological simulations where an ensemble of filaments is available, one can forgo the inspection by eye and simply use the closest pair of galaxies with similar masses which are linked by the skeleton as the starting and end points of a filament.

<sup>4</sup>This value is lower than 200 times the critical density of the Universe which is commonly used in the literature to define virialized structures. This reflects the fact that the density of haloes at the virial radius is lower than their average density by about a factor 3.

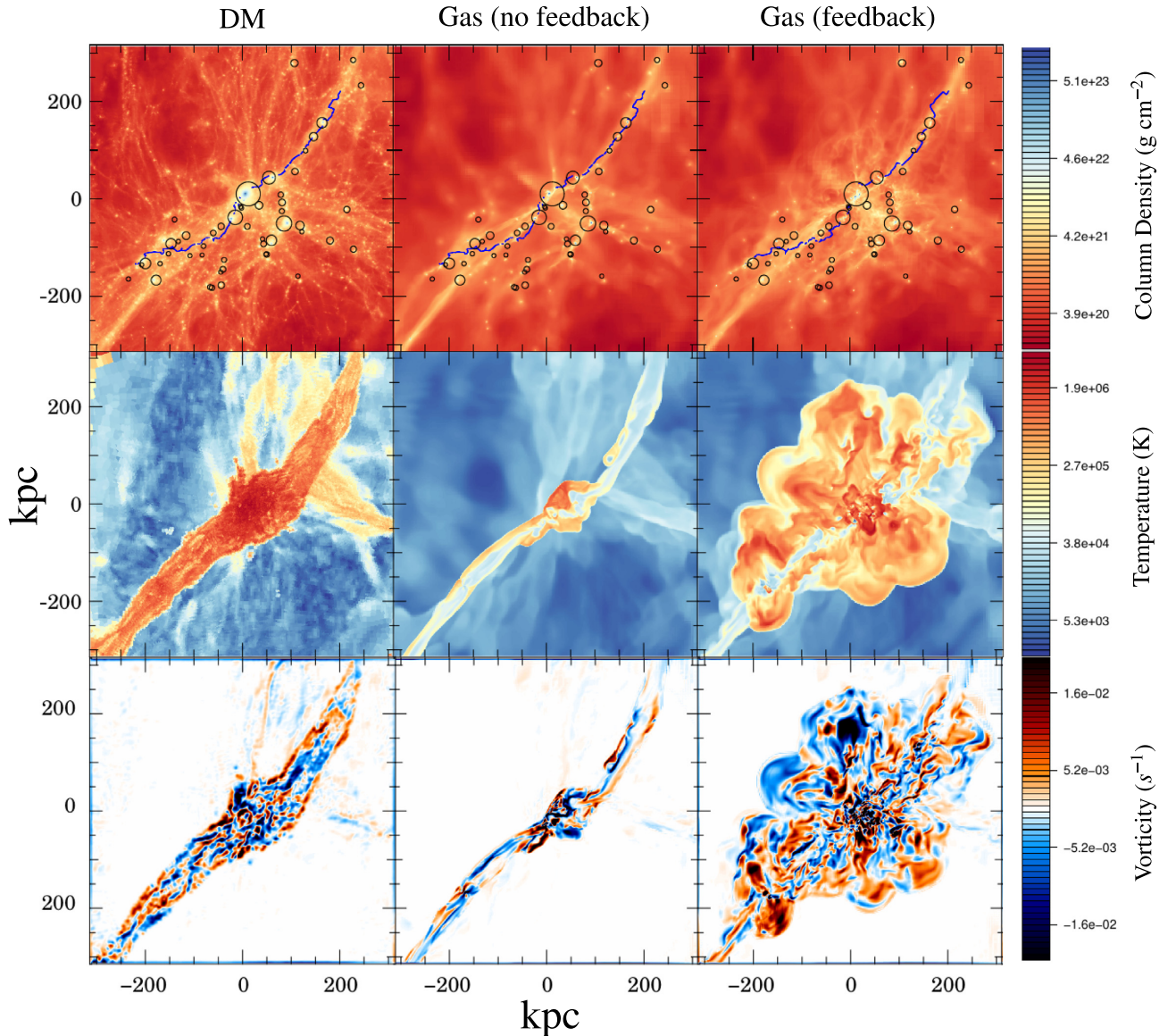


**Figure 3.** DM (left-hand column) and gas (no-feedback run, middle column; feedback run, right-hand column), with each row showing column density (top), temperature (middle), and vorticity (bottom) in a slice 625 kpc across and 1 kpc thick at  $z = 4$ . The main filament, as extracted from the DM density field, is overplotted (blue solid line) on the column density maps. The virial radii of the 50 largest haloes are marked as circles. The differences between the feedback and no-feedback skeletons are caused by small differences in the noise level associated with DM particles: they yield slightly different paths which have a very similar length, so that either path can be chosen by the algorithm described in the text. The colour bar for the density represents the gas. To estimate it for the DM, one simply needs to divide the numbers shown by the universal baryon fraction. For the DM temperature, velocity dispersion is used as a proxy, with dark blue corresponding to regions of  $\sim 0.02 \text{ km s}^{-1}$  and deep red with  $\sim 100 \text{ km s}^{-1}$ . In the vorticity panels, red represents matter swirling counter clockwise around the filament, and blue is for matter rotating in the opposite direction.

exact way that segments connect, resulting in the algorithm picking one of these paths in one run and the other path in the other run. Our results are, by and large, independent of such small randomly induced differences.

## 2.3 Cross-section measurements

### 2.3.1 Calculating DM temperature and vorticity fields

Due to the discrete Lagrangian nature of the numerical technique used to evolve the DM density field, a simple cloud-in-cell interpolation on to a reasonably sized regular grid generates a non-smooth density field in poorly sampled, low-density regions. To get around this

difficulty, a Delaunay tessellation (Schaap & van de Weygaert 2000) is computed from the DM density and velocity fields (see e.g. Schaap 2007), which ensures their spatial continuity. The Delaunay grid is then projected on to a regular uniform grid, coinciding with AMR grid level 11, which corresponds to the maximum resolution mapping of the entire filament (cubic cells 1.22 kpc on a side, see Fig. 2). This uniform grid is used for measurement of all quantities in this paper unless otherwise stated. The DM velocity dispersion field – used as a proxy for temperature – is then obtained by computing the square of the difference between each particle velocity and the value of its nearest neighbour grid cell and re-applying the Delaunay tessellation with this dispersion as the weight. Every time the Delaunay tessellation is projected on



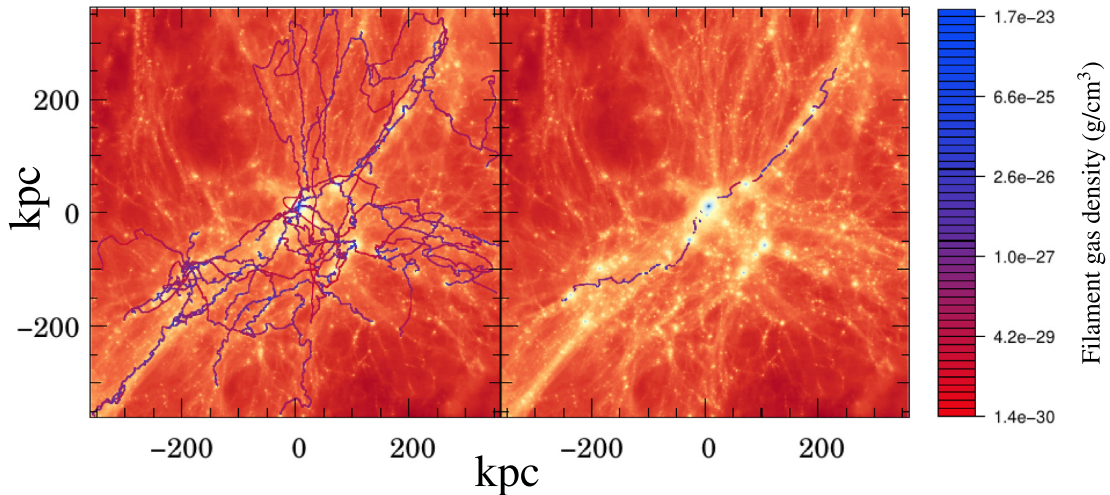


**Figure 4.** The left-hand plot shows the raw skeleton extracted by DISPERSE, which traces all the filaments of the DM density field, coloured according to the relative density (with low density in red and higher density in blue). Using Dijkstra’s algorithm, we then obtain the skeleton on the right, where we have removed filament segments from regions with densities greater than 130 times the mean density, resulting in gaps around virialized haloes and sub-haloes (indicated by circles enclosing their virial radii on Fig. 3). In both panels, the skeleton is overplotted on a  $z = 4$  projection of the DM density field.

to the grid, we average all the tetrahedra (or volume fractions of) that co-exist in each grid cell. The vorticity, on the other hand, is simply calculated by taking the curl of the velocity field on the uniform grid. As this latter is extremely noisy, a Gaussian smoothing is applied prior to computing vorticity, with a width of two cells.

### 2.3.2 Cross-section extraction and radial profiles

For each segment of the skeleton, a field (density, temperature or vorticity) is linearly interpolated in a plane, the thickness of which is equal to the skeleton segment length (typically 0.3 kpc, though this depends on the local density). This plane is perpendicular to the segment and centred on it. An example of individual cross-sections in the density, temperature, and vorticity fields is displayed in Fig. 5. Note that the position of the DM or gas density peak does not necessarily lie exactly at the centre of the plane due to the smoothing of the skeleton. Smoothing is required to ensure that individual segments point along the filament direction, and thus, that the extracted planes are truly perpendicular to the filament. The gas density maximum is not tied to the DM density maximum and thus, is also unlikely to be at the centre of the plane. In order to correct for such small offsets which nevertheless do affect profile measurements, each plane is shifted using a method similar to the ‘shrinking sphere’ method outlined in Power et al. (2003). The centre of mass of a circle centred (with a radius greater than the truncation radius) on the initial guess from DISPERSE is calculated. The circle is moved to the centre of mass before the procedure is repeated with a smaller circle. This method is more robust to the presence of additional substructure within the filament, particularly as cells with  $\rho > 40\langle\rho\rangle$  have had their density reduced to  $40\langle\rho\rangle$  for the calculation of the centre of mass. This prevents haloes existing within or near the filament from being chosen as the filament centre and distorting the filament profile. DM and gas planes are therefore translated independently. This procedure allows us to align all segments when stacking cross-sections.

Vorticity and temperature fields interpolated on to the plane perpendicular to the segments are then translated with the same

shift as the density field. When looking in the plane perpendicular to them, filaments appear as strong peaks in the projected density field (see top row of Fig. 5). Alongside this, the major walls associated with these filaments are often visible extending out from the peaks, forming thick elongated structures which are not necessarily straight. In the temperature field (middle row and column of Fig. 5), strong radial shocks are observed around the filaments themselves, with weaker shocks also present at the wall boundaries and where the walls intersect to form the filaments. In the vorticity field (bottom row, middle column of Fig. 5) both filaments and walls are identified with the regions of highest vorticity amplitude. The DM filaments (left-hand column of Figs 3 and 5) appear wider than their gaseous counterparts. Supernovae feedback (right-hand column of Figs 3 and 5) renders filaments and walls imperceptible in the gas vorticity field (bottom right-hand panels), although radial shocks are still present at the filament edges (middle right-hand panel) and the gas density peak remains clearly visible (top right-hand panel).

Radial profiles are measured from the 2D cross-sections by computing the azimuthal average in concentric shells centred on the highest density point. When discussing the effects of resolution on the filament profile, we take the median value for the distribution of all filament segments at a given resolution and for each radius, as a single profile is required. However, for the rest of the measurements in this paper, we consider individual profiles fitted to each cross-section over the entire radius range. In Fig. 6, the median profile obtained in that way is indicated by the filled red disc symbols joined by the red solid line, with the  $1\sigma$  scatter around the median profile indicated by the shaded area. The advantage of this second method (fitting the whole profile) is that we can easily bin results according to other filament properties, such as distance to the central galaxy. This should more accurately reflect the underlying filament property distribution.

### 2.3.3 The special case of vorticity cross-sections

Vorticity being a vector, the structure of the vorticity field is far more complex than density or temperature (as illustrated by the

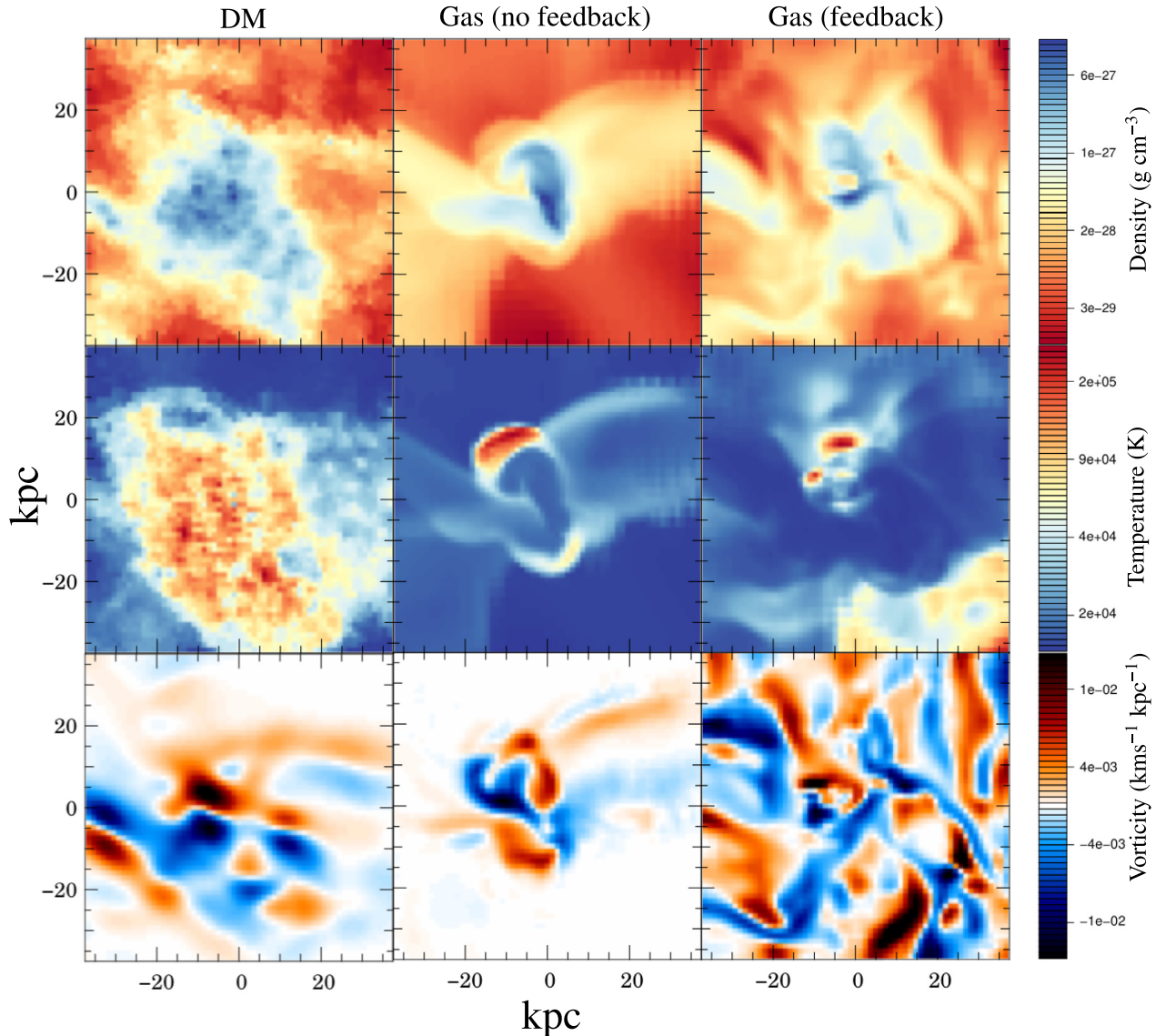


**Figure 5.** A typical filament cross-section, extracted 200 kpc away from the central galaxy in DM (left-hand column) and gas (no-feedback run, middle column; feedback run, right-hand column) at  $z = 4$ . The thickness of the slice is of order 1 kpc. Note how the central filament (density peak in the 2D slice) is embedded in a weaker wall structure (which appears as a thick elongated tube encompassing the peak). From top to bottom row: density, temperature (or velocity dispersion for DM, running from 0 to  $25 \text{ km s}^{-1}$ , dark blue to red) and vorticity along the filament, with red representing matter rotating counter-clockwise and blue in the opposite direction.

bottom panels of Figs 3 and 5) and, as a result, it not easy to stack individual vorticity profiles obtained for each skeleton segment. When stacking is required, we therefore use the modulus of the vorticity parallel to the direction of the filament and ignore azimuthal variations in vorticity. The vorticity field in the direction of the filament is extracted in the same way as described in the previous section for the density and temperature. As shown in the bottom panels of Fig. 5, the vorticity has a multipolar structure, with several rotating and counter-rotating vortices surrounding the filament. Outside the filament the amplitude of vorticity rapidly declines. Within filaments, the geometry of the vorticity field is mainly quadrupolar (see Laigle et al. 2015, though we found that dipoles and higher order structures are not uncommon reflecting that the flow have shell-crossed several times). This larger diversity in the structure of the vorticity field probably reflects the fact that the

analysis in this paper looks at smaller scale vorticity than Laigle et al. (2015) and extends the measurement to gas. We recall that primordial vorticity is destroyed in an expanding Universe, and therefore voids are extremely vorticity poor. Vorticity can later be produced by shocks or shell-crossing (respectively for gas and DM), and as result is chiefly confined to walls, filaments and nodes (see e.g. Pichon & Bernardeau 1999).

### 3 RESULTS: MEASURING THE FILAMENT PROFILES

In the following, we first derive analytically the radial profiles of filaments under the assumption that they are in hydrostatic equilibrium, and then compare them to the profiles directly measured in the simulation.



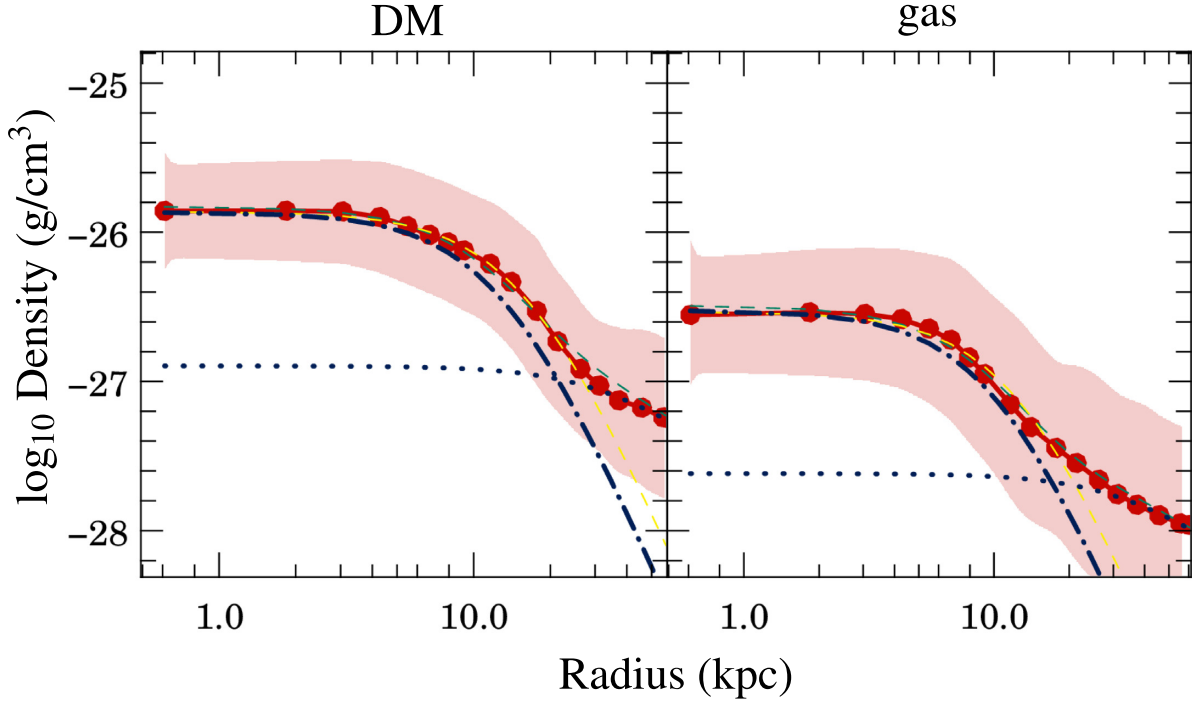


**Figure 6.** Fits of the median DM (left-hand panel) and gas (right-hand panel) density profiles (red solid line and red disc symbols) at  $z = 4$ , using a filament plus wall  $\mathcal{M}_{\text{fil}+\text{wall}}$  (green dashed line) or a filament only  $\mathcal{M}_{\text{fil}}$  (yellow dashed line) model. The blue lines shows the  $\mathcal{M}_{\text{fil}+\text{wall}}$  decomposed in the filament (dot-dashed) and wall (dotted). The shaded area represents a  $1\sigma$  deviation estimated by bootstrap re-sampling the values at each radial distance.

### 3.1 An analytic description of DM and gas filament profiles

To obtain our analytic solution, we make the simple assumption that filaments may be modelled as infinite self-gravitating isothermal cylinders. Fig. 7 presents the sound speed and velocity dispersion profiles in filaments. We have been careful to subtract the bulk velocity of the material when extracting this data. Within the filament, the sound speed and velocity dispersion are flat and dominate over the accretion velocity on to the filament, which suggests – for the centre of the filament at least – that the filament may indeed be treated as an isothermal cylinder in hydrostatic equilibrium<sup>5</sup>, i.e.

$$\nabla\phi = -\frac{\nabla P}{\rho}, \quad (1)$$

where  $P = \mathcal{K}\rho$  and  $\mathcal{K} = k_B T / (\mu m_p)$ , with  $\rho$  the density,  $T$  the temperature,  $k_B$  the Boltzmann constant,  $m_p$  the proton mass, and  $\mu$  the mean molecular weight of the gas. Stodólkiewicz (1963) solved this equation in the case of cylindrical symmetry (see also Ostriker 1964); and we will discuss the solution shortly. However, before we do, we briefly outline why it also applies to the collisionless DM fluid. Let us consider the time-independent Jeans equations (Jeans 1915) for such a collisionless system

$$\frac{\partial}{\partial x_i}(nv_i) = 0; \quad nv_i \frac{\partial v_j}{\partial x_i} = -n \frac{\partial \phi}{\partial x_j} - \frac{\partial (n\sigma_{ij}^2)}{\partial x_i}, \quad (2)$$

where  $v_i$  are the velocities,  $\sigma_{ij}$  are velocity dispersions, and  $n$  is the DM number density. Under cylindrical symmetry, we may neglect all but the radial component of these equations. Further assuming

<sup>5</sup> At least in the plane perpendicular to the filament, as we know that eventually, DM and gas flow along the filament into DM haloes. In the steady state regime however, such a flow should not perturb the equilibrium.

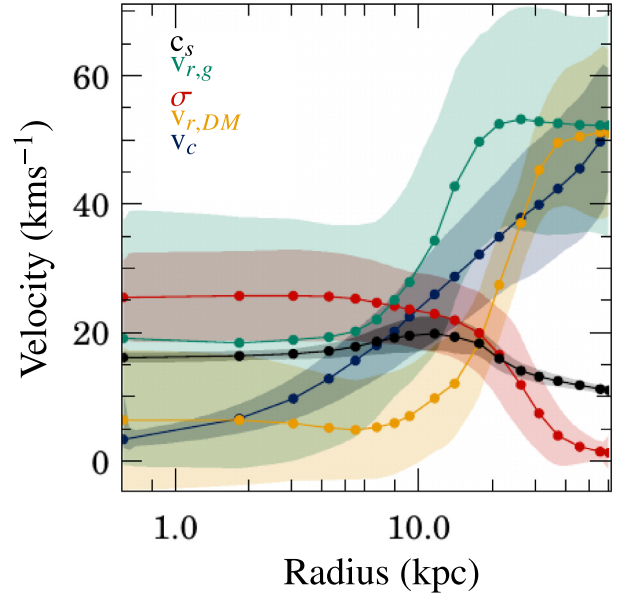


**Figure 7.** Median values for gas sound speed (black) from the no feedback run, DM velocity dispersion (red), gas (green), and DM (yellow) accretion velocity and circular velocity (blue) profiles at  $z = 4$ , with shaded regions representing the  $1\sigma$  scatter about the mode for each data point. Note that in the inner filament region, one measures a near constant sound speed and velocity dispersion, which indicates the filament is, to a large extent, isothermal. This breaks down at larger radii, due to both higher rates of radial inflow and falling sound speed and velocity dispersion.

steady state (i.e. that  $v_r = 0$ , such that accretion on to the filament is negligible compared to internal pressure support) and that velocity dispersion is isotropic, the equations simplify to

$$\frac{d}{dr}(nv_r) = 0; \quad \frac{d\phi}{dr} = -\frac{1}{n} \frac{d(n\sigma^2)}{dr}. \quad (3)$$

The second equation in (3) is entirely analogous to equation (1), with  $\mathcal{K} = \sigma^2$ , though it is clear that accretion flow on to the filament cannot be ignored at large radii (see Fig. 7). The solution to both equations is therefore that given by Stodólkiewicz (1963)

$$\rho(r) = \frac{\rho_0}{(1 + (r/r_0)^2)^2} \quad \text{with} \quad r_0 = \sqrt{\frac{2\mathcal{K}}{\pi G \rho_0}}, \quad (4)$$

where  $G$  is Newton's gravitational constant,  $\rho_0$  is the central density, and  $r_0$  the core radius of the filament. Note, however, that it is the gravitational potential common to both components which should appear on the left-hand side in both the second equation in (3) and in equation (1), so that technically speaking only the DM is truly close to a self-gravitating isothermal cylinder, the gas being in hydrostatic equilibrium in the potential well of the DM filament.

As a preliminary test of the model, we can use a typical DM filament central density of  $\rho_0 \sim 1.7 \times 10^{-26} \text{ g cm}^{-3}$ , i.e.  $\sim 100$  times the mean density of the Universe (central filament density is subject to significant variations but this is typical of the median DM density, see left-hand panel of Fig. 6 at  $z = 4$  for our choice of cosmological parameters, and a velocity dispersion  $\sigma \sim 10 \text{ km s}^{-1}$  (typical of the median DM velocity dispersion that we measure, see Fig. 7). Plugging these values in the second equation (4), we find a scale radius  $r_0 \sim 8 \text{ kpc}$ , which is broadly in agreement with the typical radius of the inner profile measured in the simulation, as shown in Fig. 6 (left-hand panel) and in Table A1. As the width of the gas filament is set by the depth of the DM potential and the gas temperature, one needs to artificially use the DM central density for  $\rho_0$  in equation (4) rather than that of the gas to obtain an estimate of  $r_0$  for this latter (as shown on Fig. 6, the gas density is about a factor 5 lower than that of the DM throughout the filament, in agreement with the universal value  $\Omega_{\text{DM}}/\Omega_B$ ). As the DM velocity dispersion for the particular filament that we study is comparable to the gas sound speed (i.e.  $\sim 10 \text{ km s}^{-1}$  or  $10^4 \text{ K}$ , which corresponds the bottom temperature of the cooling curve for atomic hydrogen, see Fig. 7), we expect a core radius for the gas similar to that of the DM, i.e.  $r_0 \sim 8 \text{ kpc}$ , and this indeed seems to be within a factor of 2 of the measured value (see right-hand panel of Fig. 6 and Table A1).

However, the isolated, infinite isothermal cylinder appears too highly idealized a model in at least one aspect, as can be seen by the failure of the yellow dashed curves (best fit obtained using the first equation 4) to match the measured median profiles (solid red lines and red disc symbols) in Fig. 6. In reality, filaments are born from the intersection of walls (see Fig. 5 middle column panels), the presence of which will modify the filament profile, especially in the outer regions. Assuming that these walls may also be treated as hydrostatic atmospheres, but this time confined to a plane containing the filament, the equations governing their profiles are identical to equations (1) and (3). These latter simply need to be solved in 1D instead of 2D, yielding in the direction  $y$  perpendicular to the plane (Spitzer 1978)

$$\rho(y) = \rho_{y0} \text{sech}^2(y/h), \quad (5)$$

with the scale height  $h = \sqrt{\mathcal{K}/(2\pi G \rho_{y0})}$ , taking a very similar functional form as  $r_0$  in equation (4) and  $\rho_{y0}$  standing for the density in the mid-plane ( $y = 0$ ) of the wall. However, we need to integrate

this wall profile over concentric cylindrical shells to evaluate how it modifies the filament profile. Unfortunately, this integral does not possess a simple analytic closed form, so we approximate the azimuthally averaged density of the wall by

$$\rho(r) = \frac{\rho_{y0}}{\alpha} \frac{\tanh(\alpha r/h)}{r/h},$$

with  $\alpha = \pi/2$ . Such an approximation captures the asymptotic behaviour of the correct solution for  $r \gg h$  and is accurate to better than 14 per cent for all values of  $r$ . As can be seen in Fig. 6, the inclusion of a wall modifies the shape of the outer filament. This might (at least partially) explain the discrepancy between filament density profiles previously reported in the literature, with power-law slopes ranging between  $-1$  and  $-2$  (see e.g. Colberg et al. 2005; Dolag et al. 2006; Aragón-Calvo et al. 2010). However, we caution that these studies were performed on much larger scales and so may not be directly comparable to our work as they might potentially be affected by different biases.

One can easily show that in the case where the gas isothermal sound speed  $c_s = \sqrt{k_B T/(\mu m_p)}$  equals the DM dispersion velocity  $\sigma$ , the density profiles of the gas and DM have the same exact shape, differing only by their normalization, i.e. the value of the central density. In the more general case where these two velocities differ, one can write the gas density profile

$$\rho_g(r) = \rho_{g0} (1 + (r/r_0)^2)^{-2\sigma^2/c_s^2},$$

so that if  $c_s > \sigma$ , it is shallower than that of the DM and vice-versa. Katz et al. (2019) measured this effect by comparing two versions of the same cosmological simulation with and without reionization. They find that narrow streams are widened by the photoheating of the gas and that the gas counterparts of the lightest DM filaments can even be entirely erased.

Note that this reasoning also applies to the isothermal gas density profile of a DM dominated isolated wall: when  $c_s$  and  $\sigma$  differ, it becomes

$$\rho_g(y) = \rho_{gy0} \text{sech}^{2\sigma^2/c_s^2}(y/h).$$

### 3.2 Testing the simple model

The first assumption we have made concerns the isothermality of the filament-wall system and that accretion on to the filament provides it with negligible support. In Fig. 7, we can see that for the no feedback run, both the gas sound speed (black solid line and solid disc symbols) and the DM velocity dispersion (red solid line and solid disc symbols) stay constant over most of the width of the filament, indicating that the isothermal approximation does indeed hold rather well. In addition, the gas and DM accretion velocities are considerably lower than the sound speed and velocity dispersion, respectively, and as such the dynamics of the system should be mainly driven by the pressure support. Moreover, the accretion shock itself is also non-adiabatic. Indeed, the upstream Mach number (beyond 20 kpc) is  $\mathcal{M}_u \approx 50/10 = 5$ , thus, the Rankine–Hugoniot jump conditions lead to a downstream Mach number  $\mathcal{M}_d = 0.47$ , and it, thus, follows that the downstream sound speed (within 10 kpc of filament centre) should be  $40 \text{ km s}^{-1}$ , i.e. twice the value of that measured. This indicates that the filament accretion shock is radiative rather than adiabatic. Finally, we also plot on Fig. 7, the circular velocity  $V_c \equiv (GM/r)^{1/2}$  (blue solid line with solid disc symbols) measured for the filament, where  $M$  is the mass enclosed by a cylindrical shell of radius  $r$ . We find that it is comparable to or lower than the sound speed/velocity dispersion, which further indicates that the filament

is chiefly supported by pressure rather than by rotation, contrarily to what is argued in Mandelker et al. (2018).

In Fig. 6, we present two models, pure filament ( $\mathcal{M}_{\text{fil}}$ ) and filament with wall ( $\mathcal{M}_{\text{fil+wall}}$ ). In practice, this means that along each individual skeleton segment, we fit the radial density using the formula

$$\rho(r) = \frac{\rho_0}{(1 + (r/r_0)^2)^2} + \rho_1 \tanh(\alpha r/r_1) \frac{r_1}{r}, \quad (6)$$

where  $r_1 = h$ , and  $\rho_1 = \rho_{y0} \alpha^{-1}$ . In principle, the values for  $\sigma$  and  $c_s$  could be different for the wall and embedded filament. However, for sake of simplicity and since we expect these two quantities to roughly behave in a similar manner, at least in the vicinity of the filament, we ignore the possible change in the ratio of  $\sigma^2/c_s^2$  in our  $\mathcal{M}_{\text{fil+wall}}$  model (see Fig. 7 for the validity of this assumption). The fit is performed using the Levenberg–Marquardt algorithm where the wall is first fit to the outer half of the profile with the filament contribution set to zero. The wall parameters are then frozen in place while fitting the filament parameters. In the case of a pure filament model (i.e.  $\mathcal{M}_{\text{fil}}$ ), the filament is fit to the entire profile, setting  $\rho_1 = 0$ . The procedure was tested by applying it to a sample of artificial profiles, which typically returned radii within one cell of the input radius, but does break down when the filament is too wide (i.e. extends into the region where the wall is fitted). While this is a suitable range for the purposes of this paper, filaments continue to grow as time progresses and this method may become unsuitable at later times. In Fig. 6, we show how each of the two models fares against the measured median density profile of the DM (left-hand panel) or gas (right-hand panel) at  $z = 4$ . Errors on the radius are estimated by considering the full distribution of density profiles measured from individual skeleton segments and fitting this distribution with the best matched normal distribution to evaluate the value of the standard deviation. For errors on the density, we use the best matched lognormal distribution instead, which is better suited to density distributions in filaments (see e.g. Cautun et al. 2014).

Looking at Fig. 6, it is not possible to distinguish the two models,  $\mathcal{M}_{\text{fil+wall}}$  (green curve) and  $\mathcal{M}_{\text{fil}}$  (yellow curve), in the inner region ( $r \leq 20$  kpc). When the profiles are stacked as in this figure, the fits work equally well with or without the wall. However the size of the core radius that these models return are very different when considering individual profiles:  $r_0 = 19.34 \pm 7.15$  kpc for  $\mathcal{M}_{\text{fil}}$  compared to  $r_0 = 8.39 \pm 3.82$  kpc for  $\mathcal{M}_{\text{fil+wall}}$  for the DM filament. This factor of 2 discrepancy is also present for the gas filament:  $r_0 = 8.99 \pm 1.86$  kpc for  $\mathcal{M}_{\text{fil}}$  compared to  $r_0 = 5.04 \pm 1.96$  kpc for  $\mathcal{M}_{\text{fil+wall}}$ . The core radii given by the  $\mathcal{M}_{\text{fil}}$  model can be rejected by simple visual inspection of Fig. 3: they are comparable to the outer edge radius of the filaments.

Although we only show the  $z = 4$  median profiles, this behaviour of the two models holds for all redshift outputs examined in this work (see Table A1 for a list).

We now discuss how each model fits individual cross-section density profiles (examples of these are shown as thin dashed curves on Fig. 6) rather than the median. In this case, errors on the density are estimated by calculating the gradient of the density profile and multiplying it by the spatial resolution (size of cell). For the DM density, a Poisson noise contribution is also added in quadrature to the error estimate. We plot in Fig. 8 the corresponding distributions of reduced  $\chi^2_v$  which peaks at 3 for the DM density profile and 0.5 for the gas in the preferred model  $\mathcal{M}_{\text{fil+wall}}$  (dashed and solid green lines in Fig. 8, respectively). For the  $\mathcal{M}_{\text{fil}}$  model, these same distributions are much less strongly peaked around  $\chi^2_v = 6$  and 4 for the DM and gas density profiles, respectively (dashed and solid yellow curves).

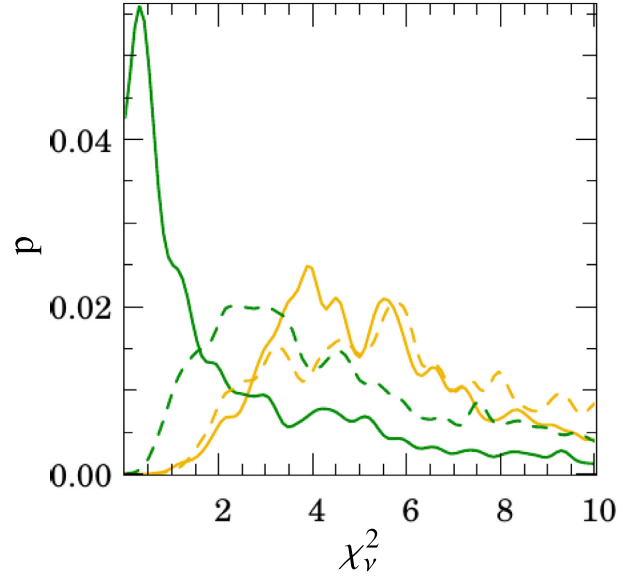


**Figure 8.** Normalized distributions of reduced  $\chi^2_v$  obtained when fitting the filament only (yellow) or filament plus wall (green) models to filament density projections in individual slices perpendicular to each skeleton segment at  $z = 4$  (see text for detail). The gas filament is represented by the solid curves, whilst the DM counterpart is shown as dashed lines.

Note that the measurement errors are relatively large, especially at the centre of the filament for the gas and overall for the DM because of a significant Poisson noise contribution. Though these values of  $\chi^2$  suggest a fit to the simulation data which lies somewhat on the poor side, it is unclear that the validity of the model should be measured by  $\chi^2$  statistics in the first place. Indeed individual profiles deviations from the model are very likely correlated with one another when substructures residing within the filament perturb its density field.

For sake of completeness, let us mention that at  $z = 4$ , the fits of the full set of skeleton segments using the  $\mathcal{M}_{\text{fil+wall}}$  model to the DM component for the no feedback run returns  $r_0 = 8.39 \pm 3.82$  kpc as the mode and width of the fitted Gaussian for the core radius of the filament (as previously mentioned) and  $r_1 = 6.79 \pm 2.80$  kpc for the scale height of the wall. Similarly, we fit a lognormal distribution to the DM central densities to obtain  $\log_{10}(\rho_0/\text{g cm}^{-3}) = -25.83 \pm 0.49$  for the filament and  $\log_{10}(\rho_1/\text{g cm}^{-3}) = -26.45 \pm 0.45$  for the wall. As for the gas, we obtain  $r_0 = 5.04 \pm 1.96$  kpc and  $r_1 = 7.70 \pm 3.00$  kpc, with densities of  $\log_{10}(\rho_0/\text{g cm}^{-3}) = -26.53 \pm 0.45$  and  $\log_{10}(\rho_1/\text{g cm}^{-3}) = -27.12 \pm 0.37$ . A list of values for the filament radii and densities at other redshifts is provided in Tables A1 and A3.

As gas filament temperature remains around  $10^4$  K at all times after re-ionization, their density profile flattens rapidly as the mass of their DM counterpart decreases and the sound speed approaches the critical value of  $c_s = \sqrt{2}\sigma$ . This means that low-mass filaments will only exist in the DM component (compare the top left-hand and middle panels in Fig. 3), as a  $10^4$  K gas has too much pressure to be trapped in the DM potential well in that case, and thus, talking about a gas  $r_0$  becomes quite meaningless. On the other side of the mass range, we expect more massive filaments, where DM has a larger velocity dispersion, to have better defined cores in the gas than DM, as this former should still radiatively cool down to  $\sim 10^4$  K and thus have a much steeper density profile than its DM counterpart. As a result of this cooling, it is possible that the central gas density of massive filaments will become comparable to that of the DM, in which case



our assumption that the DM sets the gravitational potential would cease to be valid and the core radii of the two components might then differ substantially. However, for the filament system considered in this paper, the approximation of similar DM and gas density profiles seems to hold quite well (see Fig. 6).

In light of the previous discussion, we interpret the difference between the measured and predicted median values of  $r_0$  as a departure from the isothermal/hydrostatic approximations for the filament (see Fig. 9, middle panels), rather than to asymmetry or a systematic variation of core size as a function of distance to the galaxy (see section 11 for more detail concerning this latter variation). For the DM, the filament median velocity dispersion varies by 10 per cent within  $\sim 2$ –3 core radii. For the gas, where a shock is clearly visible around 15 kpc away from the centre of the filament (middle right-hand panel of Fig. 9), the temperature varies by less than 60 per cent between the centre of the filament and the maximum of the shock.

These discrepancies notwithstanding, it is striking how filaments in our cosmological simulations resemble those obtained in a much more idealized set-up with similar resolution presented in Klar & Mücke (2012). More specifically, even though these authors ignore the DM component as well as the fragmentation and mergers of filaments, they find that their gaseous linear structures are in radial hydrostatic equilibrium and exhibit an isothermal core several kpc wide with central densities and temperatures remarkably similar to those we measure in a more realistic context. They also identify an outer shocked region with similar properties as ours, but with a gravitational focusing which reduces  $r_0$  and increases  $\rho_0$  as the filament approaches the DM halo to which it is connected. As previously mentioned, we will come back to this latter point in section 3.4 of our results devoted to the temporal and spatial evolution of filament properties, but already note that such a focusing effect is not as pronounced in our simulations.

### 3.3 Vorticity, temperature, and the radial extent of filaments

Having extracted the main filament from the simulation and measured the characteristic radius of its core through the use of a simplified model of hydrostatic equilibrium for its density profile, we now turn to the question of determining its outer size, or *truncation* radius, as the analytic profile cannot extend to infinity in the radial direction.

Beyond a certain radius, it is no longer true that sound and dispersion velocities dominate over the accretion velocity, as can be seen in Fig. 7. A failure of the hydrostatic model will thus occur, leading to a potential definition of the truncation radius, which also coincides with the position of the accretion shock on to the filament for the gas. We have opted not to use the peak temperature position as a definition of the truncation radius, as individual skeleton segment profiles, both in temperature and vorticity are often asymmetric and/or distorted by their environment, and may contain multiple peaks when averaged over concentric radial shells as a result (see Fig. 5 for an example). Moreover, such a definition would not apply to DM velocity dispersion profiles. We have therefore chosen to use a universal method for all physical quantities and types of filament (gas or DM), which also has the benefit of providing internal consistency between measurements. We, thus, define the truncation radius as the point where the steepest descent in the temperature/vorticity/velocity dispersion profile is attained. In the DM, this is analogous to the splashback radius for haloes as defined in Diemer et al. (2017), as vorticity and velocity dispersion is only generated in the DM where shell crossing has occurred. At  $z = 4$ , this yields a truncation radius of  $18.6 \pm 4.0$  kpc for the gas temperature profile, while the gas vorticity profile gives  $21.7 \pm 6.6$  kpc. The DM filament at the same redshift

has a measured truncation radius of  $28.6 \pm 6.5$  kpc when using the velocity dispersion profile and  $25.9 \pm 4.5$  kpc if we consider its vorticity profile (see Table A1). It is interesting to note that the accretion shock of the gas filament seems positioned well within the DM filament (roughly at half the DM truncation radius). In order to check the robustness of these measurements vis-à-vis resolution, the data was extracted at four different spatial resolutions. Note that this is *not* a study where we change the resolution and re-run the simulation, but simply a post-processing of the *same* simulation at different resolutions, so we expect to achieve better agreement than if we had done a proper resolution study. As resolution increases progressively from 10 to 1.22 kpc (level 8 to 11), the profiles are seen to converge across every panel of Fig. 9. Note that for comparison, our *lowest* level of resolution, i.e. 10 kpc roughly corresponds to the *highest* level of resolution available to capture filaments in current cosmological simulations with volumes on the order of 100 Mpc on the side, like Mare Nostrum (Ocvirk et al. 2008), Horizon-AGN (Dubois et al. 2014), MassiveBlackII (Khandai et al. 2015), Eagle (Schaye et al. 2015), IllustrisTNG (Nelson et al. 2018), or SIMBA (Davé et al. 2019).

Looking first at the density profiles both of the DM and gas filaments (top panels of Fig. 9), one can see that in going from the highest resolution level to the lowest one, the central density (inside the core) is underestimated by about an order of magnitude, and one becomes unable to measure the core radius of the profile with a reasonable accuracy. On the other hand, the DM velocity dispersion profiles (middle left-hand panel of Fig. 9) seem to converge faster than the density ones, with the lower resolution estimates compatible with the higher resolution ones at all radii. This seemingly rapid convergence is induced by the shape of the isothermal profiles which are, by definition, flat, especially in the case of the DM. For the gas (middle right-hand panel of Fig. 9), the temperature does not show as marked a convergence as the DM velocity dispersion because of the presence of the accretion shock: the low-resolution data (black curve), which barely resolves the truncation radius of the filament underestimates the shock temperature and overestimates the core temperature by a similar amount. Having said that, the shock position is fairly robust to resolution changes despite being radially asymmetric, which leads to its ‘smearing’. A minimum resolution of 2.4 kpc is required to correctly capture both the temperature of the accretion shock and that of the gas filament core.

### 3.4 Evolution of filament profiles over cosmic time and distance from central halo

Having focused, so far, the discussion of the filament profile at  $z = 4$ , we now address the issue of its temporal evolution. Since  $r_0 = \sqrt{2K/\pi G \rho_0}$ , we naively expect that  $r_0 \propto (1+z)^{-3/2}$ , provided the filament central density scales with that of the background Universe – which we measure to be the case (see Table A3) – and its central temperature/velocity dispersion remain roughly constant with redshift. Conversely, we can deduce the scaling of filament temperature/velocity dispersion with redshift by measuring the departure of  $r_0$  from this specific power-law scaling. In our simulation, we find that for the gaseous filament, the central radius grows as  $r_0 \propto (1+z)^{-2.72 \pm 0.26}$ , which means that the sound speed should scale like  $c_s \propto (1+z)^{-1.22 \pm 0.12}$  whereas we measure  $c_s \propto (1+z)^{-1.41 \pm 0.28}$ , i.e. an evolution quite consistent with the naive expectation.

For the DM filament counterpart, the growth of  $r_0$  is faster, with a measurement of  $r_0 \propto (1+z)^{-3.18 \pm 0.28}$  (see Fig. 10), a faster rate than the approximate size of the central galaxy ( $r_{\text{gal}} = 0.2r_{\text{vir}}$ , blue solid

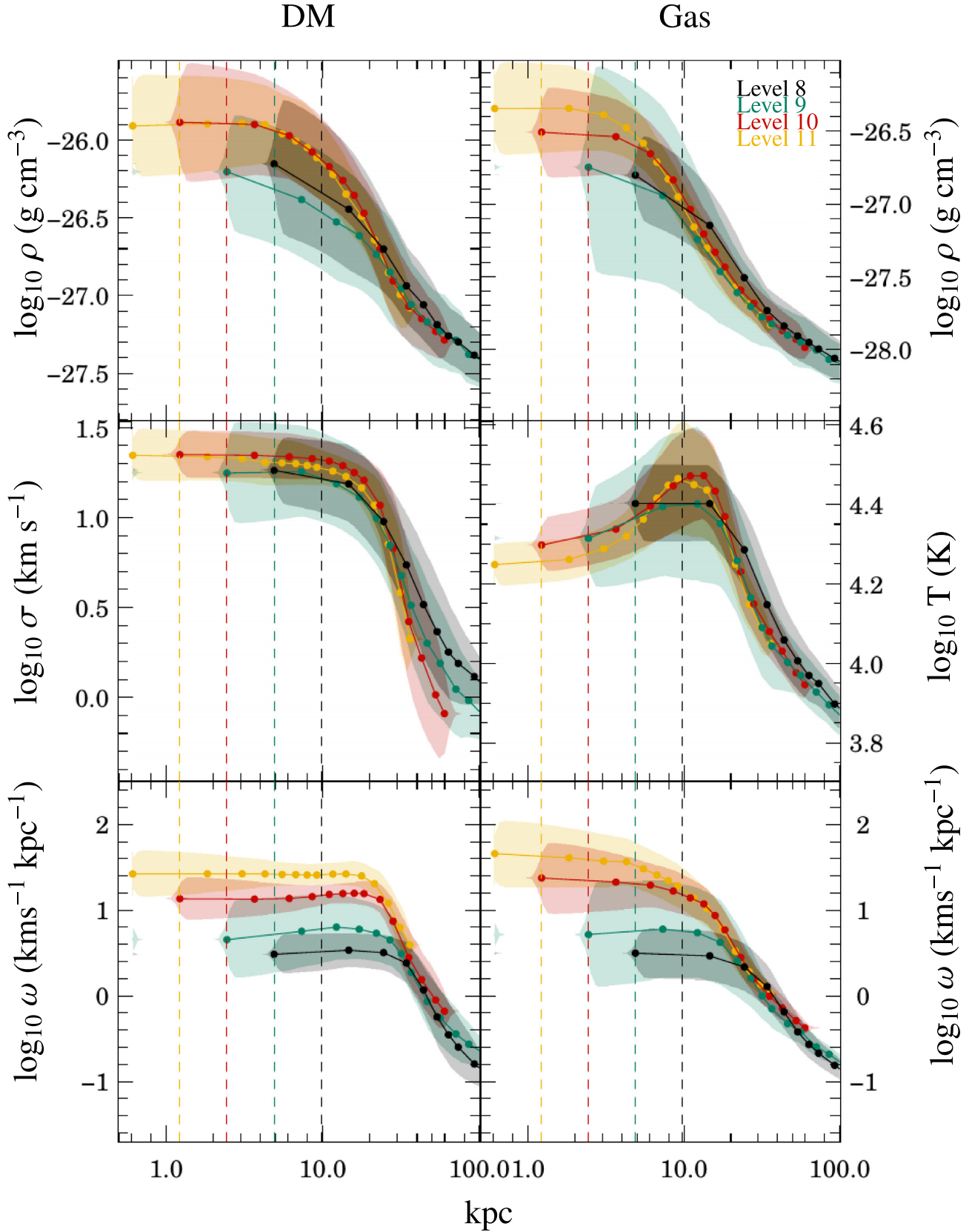


**Figure 9.** The median radial profiles of the filaments in DM (left-hand column) and gas in the no-feedback run (right-hand column), for density (top row), temperature (middle row), and vorticity (bottom row) at  $z = 4$ . Displayed profiles (from black to yellow) represent data extracted at different spatial resolutions of the AMR simulation grid (vertical dashed lines or levels 8 to 11, respectively, see text for detail). Error bars are generated by bootstrapping the distribution of individual filaments profiles and taking the root mean square at each radius.

line on the figure). This implies that  $\sigma \propto (1+z)^{-1.68 \pm 0.15}$  as redshift decreases, whereas we measure in the simulation that  $\sigma$  scales as  $(1+z)^{-1.46 \pm 0.39}$ . The evolution of both gas and DM filament core radii are therefore consistent with the naive expectation at a  $\sim 1\sigma$  confidence level. Strictly speaking, any evolution of the central sound speed and velocity dispersion is in contradiction with the underlying assumption of isothermality used to derive the filament profiles, as this latter requires *no* change in either quantity with redshift. However, as the evolution is slow compared to the sound crossing time of the central region, an instantaneous isothermal profile fits the data fairly well.

The explanation for the somewhat faster growth of the core radius of the filaments than the radius of the central halo to which it is connected is that the 'old' core material is preferentially drained by haloes residing within the filament, while a 'new' core forms out of more freshly accreted matter on to the filament (see e.g. Pichon et al. 2011). As a result, the filament core radius is more sensitive to the recent accretion history on to the filament than the halo. Such a behaviour is reminiscent, at least qualitatively, to that of the Navarro–Frenk–White density profile scale radius,  $r_s$ , found by e.g. Muñoz-Cuartas et al. (2011) whose time evolution also differs significantly from that of the virial radius of the DM halo (except in that case it is the opposite:  $r_s$ , which is less sensitive to the halo recent accretion history, starts decreasing with redshift earlier than  $r_{\text{vir}}$ , see their Fig. 5). As the gas can be considered, to first order, in hydrostatic equilibrium in the DM filament potential well, we expect the evolution of its core radius to be somewhat influenced by that of the DM, i.e. that its growth also be sped up. We intend to explore this effect in more detail and with a larger sample of filaments to better assess the universality of this behaviour.

As for the truncation radius for the gas/DM filaments, determined from either the vorticity or the temperature/velocity dispersion, it represents the locus where fresh material is accreting, and as such is the rough equivalent of the halo virial radius. Fig. 10 shows the evolution of this radius as a function of redshift, along with the size of the main halo embedded in the filament ( $r_{\text{vir}}$ , orange solid line). For the DM filament, the truncation radius evolves as  $r_w \propto (1+z)^{-1.99 \pm 0.09}$  or  $r_T \propto (1+z)^{-2.16 \pm 0.12}$ , depending on whether one uses vorticity or velocity dispersion to define it. This is a growth rate very similar to that of the halo size  $r_{\text{vir}} \propto (1+z)^{-2.11 \pm 0.02}$  in this range of redshifts. However, the gas truncation radius, either derived from the vorticity or temperature of the gas filament which scale as  $r_w \propto (1+z)^{-2.85 \pm 0.17}$  and  $r_T \propto (1+z)^{-3.36 \pm 0.12}$ , respectively, grows significantly faster than its DM counterpart. This is reminiscent of the stability driven argument for the propagation of a radiative shock within DM haloes advanced by Birnboim & Dekel (2003), but this time applied to the filament: as time progresses and density drops, the shock is able to propagate outwards and ends up filling the entire DM filament volume. Practically, this means that even though the gas filament starts off being smaller than the central halo embedded within it (see Fig. 10) at high redshift, the truncation radius rapidly catches up with the virial radius. In our specific case, they are essentially the same size by  $z = 3.5$ .

We now go back to  $z = 4$  to explore the effect of distance to the galaxy on the width of the filament. As can be seen in Fig. 11 (top panel), both the core and truncation radii of the gas filament decrease by less than a factor 2 as a function of the distance to the main galaxy embedded within it. This decrease is progressive, from a maximum radius at 300 kpc away, which corresponds to the distance of either ends of the filament (see Fig. 1), to the virial radius of the central galaxy. We caution the reader that this is somewhat different to the

reported behaviour of the filament once it enters the virial radius of the embedded DM halo (e.g. Danovich et al. 2012). Indeed, within the virial radius, one expects the gas filament to undergo more important gravitational focusing (Klar & Mücke 2012). The reason why this does not happen as strongly in our case very likely has to do with the fact that, as previously mentioned, we chose to excise embedded DM haloes to focus our analysis on filament properties. However, while the filament radii do not decrease much as the gas approaches the halo, it is still enough to increase the central density, rising by a factor of approximately 5 (dark solid line and symbols in the bottom panel of Fig. 11). Note that such a behaviour is not specific to the gas as the DM central density (green solid line in the bottom panel of Fig. 11) undergoes a similar change with distance to the galaxy, which is consistent with an interpretation in terms of mild gravitational focusing but also of the progressive draining of the filament core draining by the halo, as previously mentioned. Finally, we want to emphasize that the NUT galaxy, essentially connected to one (two if counting each direction as an individual object) filament(s) could be somewhat of a peculiar case. Once again, further high resolution work on a much larger sample of filament/galaxies is required to properly investigate the influence of connectivity and/or halo mass on the results.

### 3.5 The impact of stellar feedback on filaments

Stellar feedback has a profound impact on the region surrounding the galaxy and filament. Given enough time, the superbubbles it generates extend most of the way up the filament, as can be seen in the central and bottom right-hand panels of Fig. 3. These galactic winds inject vorticity on large scales, and as such, this physical quantity is no longer confined to the filamentary gas. Note that, in spite of this, larger scale cosmic web filaments (i.e. larger than the superbubble) could still have well defined vorticity quadrants. More importantly, vorticity in the DM filament counterpart (bottom left-hand panel of Fig. 3) remains by-and-large unaffected, to the point that we do not deem it necessary to plot it on Fig. 11 for the run with feedback.

The CGM/IGM gas is also strongly heated by this stellar feedback and so the temperature signature of the accretion shock on to the filament is lost as well, as the middle right-hand panel of Fig. 3 demonstrates. Once again, this signature survives in the velocity dispersion of the DM component (middle left-hand panel of Fig. 3). Despite such significant perturbations, the presence of a DM filament potential well coupled to the relatively high density of the gas ensures that the cooling time within the filament remains short. As a result, the filament is still visible as a cold stream cutting through the hot superbubble in the middle right-hand panel of Fig. 3.

Due to these consequent perturbations induced by the stellar feedback, we cannot use either the temperature or vorticity to define the gas filament truncation radii in the feedback run. It should also be noted that our assumption of isothermality of the filaments becomes less valid than in the no stellar feedback case as stronger temperature gradients develop between core and outer envelope. To be more specific, in the no feedback case, the temperature varies between core and truncation radius by about a factor of 2, but in the feedback case it can reach an order of magnitude. However, most of this gradient is localized in the outer parts of the filament, so that the central region retains a significantly large isothermal core. This can be understood by performing the following simple calculation. Neglecting the presence of the wall, we may integrate both the gas and DM density profiles (from equation 4) to obtain the filament



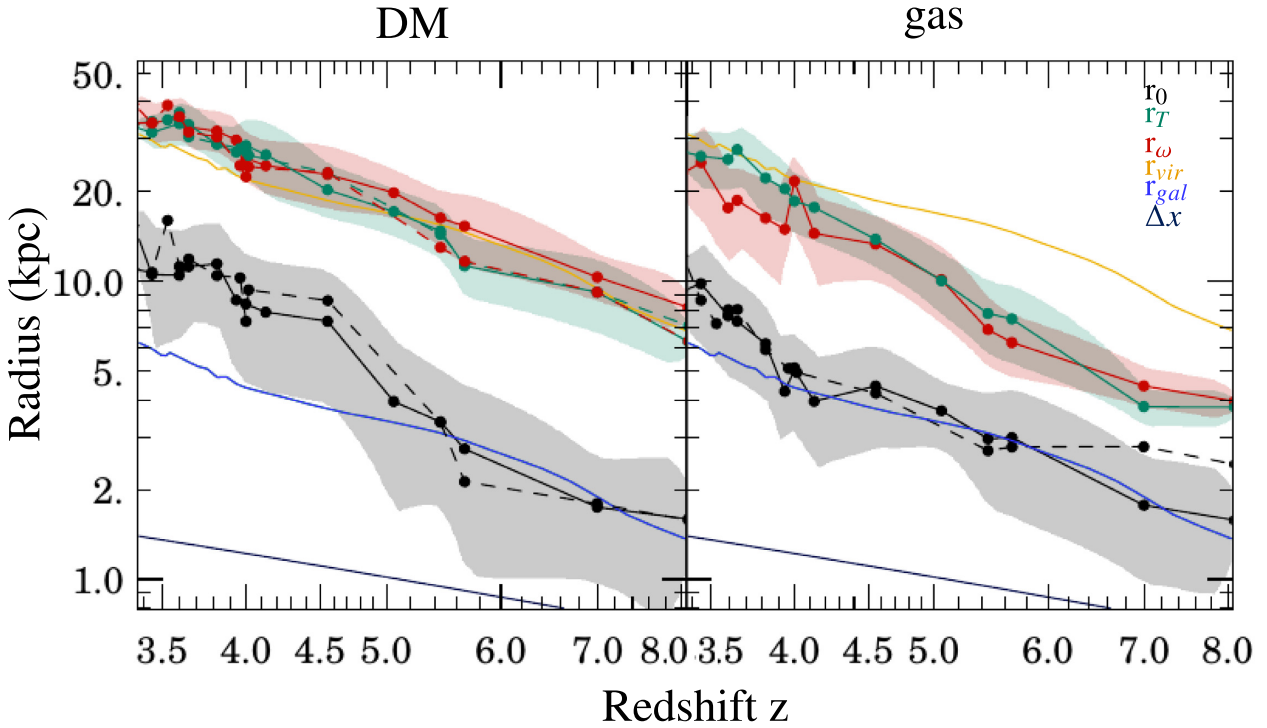


**Figure 10.** Evolution of the core (black curves) and truncation radii (red and green curves for estimates based on the vorticity and temperature, respectively) of the filaments with redshift. The left-hand panel represents the DM filament, and its gas counterpart is on the right. Dashed lines represent the feedback run. The virial radius is shown in orange and the approximate extent of the central galaxy (20 per cent of virial radius) in yellow. Finally, the spatial resolution of the simulation in the filament is indicated by the solid blue line at the bottom of each panel.

mass per unit length,  $\mu$ , and its half-mass radius

$$\mu(r) = \frac{\rho_0 \pi r^2}{1 + (r/r_0)^2} \quad \text{and} \quad r_{1/2} = r_0. \quad (7)$$

The fact that the (small) core radius contains half of the mass makes the filamentary material relatively impervious to the stellar feedback/filament interaction: provided the core is shielded from it, there can only be a minor change in the amount of gas mass that the filament carries. It has been suggested in the literature that Kelvin–Helmholtz instabilities could be triggered at the interface between cold filament gas and the feedback powered, hot, galactic wind (e.g. Mandelker et al. 2016 and subsequent work). These will depend non-trivially on redshift and the distance of a filament segment to the central galaxy, so it is quite difficult to define a unique characteristic time-scale,  $t_{\text{KH}}$ . Nevertheless, writing  $t_{\text{KH}}(r) = (r/v_w)\sqrt{\rho(r)/\rho_w}$ , where  $v_w$  is the relative velocity between the wind and the gas filament and  $\rho_w$  the density of the wind, we can see that given the steepness of the filament density profile that we measure,  $t_{\text{KH}}$  becomes larger as the perturbation progresses deeper in the filament. This means that the time-scale is ultimately set by  $t_{\text{KH}}(r_0)$ . Plugging in typical numbers for our feedback run at  $z = 4$ , i.e.  $r_0 \sim 5$  kpc,  $\rho(r_0) \sim 3 \times 10^{-27} \text{ g cm}^{-3}$ ,  $v_w \sim 100 \text{ km s}^{-1}$ , and  $\rho_w \sim 3 \times 10^{-28} \text{ g cm}^{-3}$ , we, thus, get  $t_{\text{KH}} \sim 20 \text{ Myr}$  which is about an order of magnitude shorter than the infall time from the virial radius of the embedded halo. The conclusion is, thus, that our gas filaments should not survive the interaction.

Notwithstanding that this does not happen in our simulations, which might admittedly be of too low a resolution to capture the instability properly, the calculation ignores both the importance of radiative cooling within the filament which might confine the perturbations at the surface (Vietri, Ferrara & Miniati 1997), and the

important fact that, as we have previously discussed, gas filaments are *not* self-gravitating but are located within a dominant DM filament potential well. Because of this, it is unclear as to whether Kelvin–Helmholtz instabilities can impart to the gas a radial velocity (as in perpendicular to the filament axis) larger than the escape velocity necessary to climb out of this potential well. Should they not, they would simply render the gas flow within the filament turbulent without affecting the filamentary nature of gas accretion on to haloes.

In the feedback case, we measure that the core radius of the gas filament evolves with redshift as  $r_0 \propto (1+z)^{-2.24 \pm 0.34}$ , i.e. with a scaling very similar to the no feedback run (see Fig. 10). Nevertheless, given the importance of the stellar feedback perturbations, one expects gas accretion on to the filament to be reduced in their presence. To quantify this effect, we plot the ratio of median feedback to no feedback gas density profiles along the filament as a function of redshift in Fig. 12. From the figure, one can see that while the size of core radius is not significantly affected by feedback, the central density is, to a larger extent. At  $z = 7$ , a 40 per cent reduction is measured, though this falls to 20 per cent at  $z = 3.6$ , at which point, the feedback ceases to have an effect on the filament core. We emphasize that contrary to the growth of the core/truncation radii, the impact of feedback does not scale monotonically with redshift, as it depends both on the global properties of the IGM/filament and the star formation history of the galaxy which drives the feedback. Indeed, as shown on Fig. 12, at early times ( $z \sim 8$ ), the filament core density is even *enhanced* by the action of feedback. It is possible that some of this extra gas will be entrained in the filament, but another possibility is that it will act as a shield from fresh feedback at later times. In a future paper, we plan to use tracer particles developed in Cadiou, Dubois & Pichon (2019) to distinguish between these two situations. Outside the filament, the density is seen to be enhanced

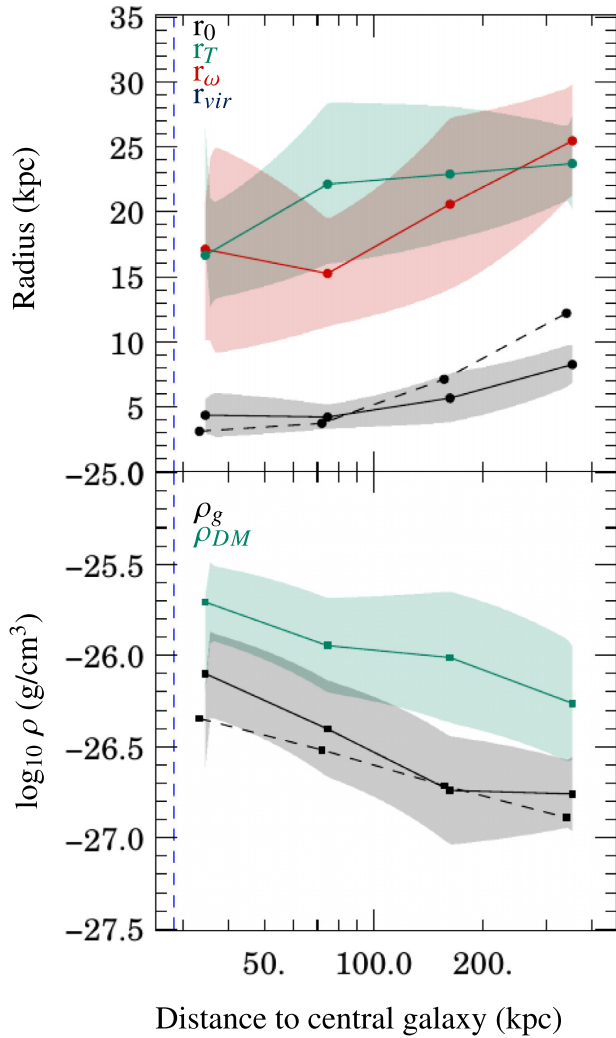


**Figure 11.** Top: gas filament radii as a function of distance to the galaxy, in the no-feedback (solid line) and feedback runs (dashed line) at  $z = 4$ . The core radius is in black, whereas the truncation radius estimated from the temperature and the vorticity profiles are in green and red, respectively. Note that the truncation radius cannot be determined from either the vorticity or temperature when feedback is included. Bottom: Central density of the filament as a function of distance to the galaxy. Gas is black, DM is green, with solid and dashed lines representing no feedback and feedback runs, respectively. The vertical blue dashed line indicates the virial radius of the halo.

in the simulation with feedback, which is somehow expected from mass conservation of the filamentary gas and the presence of the extra material brought by the galactic winds.

It should be noted that the stellar feedback implemented in our simulation is the supernova prescription of Kimm et al. (2015), which ensures that the correct energy/momentum is given to the gas irrespective of whether the Taylor–Sedov phase of the supernova is spatially resolved. As such if the filaments are not destroyed by this supernova feedback then they are unlikely to be destroyed by any ‘realistic’ supernova feedback. Yet, other types of stellar feedback are also present which could alter filament properties, whether by direct action of the feedback on the filaments or through suppression of star formation and thereby the supernova feedback (e.g. resonant scattering of Lyman alpha photons in high redshift dwarf galaxies; Kimm et al. 2018). There is, of course, photoheating

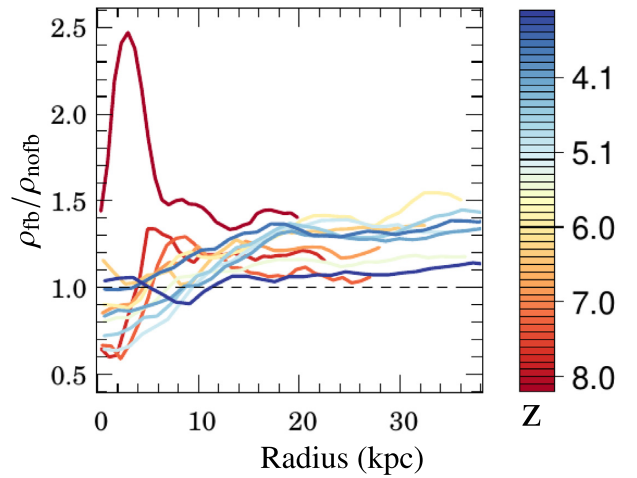


**Figure 12.** Ratio of the median gas density profiles in the feedback and no feedback runs,  $\rho_{fb}/\rho_{nofb}$ , as a function of distance to the filament centre. Curves of different colours represent different redshifts, as indicated on the figure. Very early in the simulation ( $z = 8$ ), feedback enhances the density of gas in the filament. However, at almost all other redshifts, the reverse happens: the filament is depleted of gas in the feedback run as compared to the no-feedback run. The amplitude of the effect is *not* monotonic with redshift.

due to ionizing radiation which can induce an important gas density depletion especially in filaments connecting low-mass haloes (see Katz et al. 2019 for detail). We believe that this effect is, by-and-large, captured by the UV background model implementation present in both the stellar feedback and no-feedback runs. However, another mode of stellar feedback which we do not account for, might be more effective at filament disruption as it is less confined to the galaxy: cosmic rays (see e.g. Pfrommer et al. 2017). Finally, for filaments connecting haloes of higher mass, Dubois et al. (2013) showed that AGN are also very effective at disrupting filaments and can even destroy their cores.

## 4 CONCLUSIONS

Theory suggests (e.g. Kereš et al. 2005; Dekel & Birnboim 2006; Pichon et al. 2011) that filaments play an extremely important role in the evolution of galaxies at high redshift. However, their basic characteristics are, as yet, not completely understood, and they are extremely hard to detect observationally. We used a suite of high resolution cosmological zoom-in simulations, progressively including more of the relevant physics, to place constraints on the physical properties of such a filament, from large (Mpc) scales to the point where it connects to the virial sphere of the central galaxy. Our main findings are as follows

(i) The filament in both DM and gas simulations can be described fairly accurately by a universal density profile  $\rho = \frac{\rho_0}{(1+(r/r_0)^2)^2}$  corresponding to a cylinder in isothermal equilibrium.

(ii) The filament core radius evolves for the gas grows as  $r_0 \propto (1+z)^{-2.72 \pm 0.26}$ , with the DM filament core evolving as  $r_0 \propto (1+z)^{-3.18 \pm 0.28}$ . This evolution of  $r_0$  for the gas closely tracks that of the size of the galaxy ( $0.2r_{vir}$ ).

(iii) The filament has a second characteristic radius, the truncation radius, which is detectable (at least in simulations) in the temperature/velocity dispersion or vorticity fields. This radius scales as  $r_{tr} \propto (1+z)^{-2.07 \pm 0.07}$  for DM and  $r_{tr} \propto (1+z)^{-3.10 \pm 0.10}$  for the gas. The

DM truncation radius closely matches the virial radius of the galaxy. The gas truncation radius is generally thinner at early times.

(iv) The filament properties are mildly affected by stellar feedback from the central galaxy. The core radius of the gas filament hardly changes, but its central density is generally reduced by  $\sim 20$ – $30$  percent, but this does not happen monotonically with redshift. The DM filament properties hardly undergo any change.

Our simulations also establish that filaments need to be resolved with a minimum of  $\sim 2$  kpc for a Milky Way sized halo in order to capture the filament properties. This might have important consequences for the angular momentum content of the gas transported to the galaxy. Still higher resolution will be required to capture the filaments around dwarf galaxies, though these are far more vulnerable to photoionization and so probably do not need to be resolved in detail beyond  $z = 6$ . While the mass brought by the inflowing filament gas is affected to a level of  $\sim 20$ – $30$  percent as a result of stellar feedback from the central galaxy, a further reduction is likely to occur as the filament enters the virial radius. We plan to tackle this issue using tracer particles in the near future. The interaction of the filament with galactic winds and the virialized halo hot atmosphere will also be a function of the halo mass, and therefore our results need to be extended to a larger sample.

Indeed, our analysis was performed on the filament feeding one galaxy at high resolution. We, thus, plan to apply the techniques developed in this paper to the NEW-HORIZON simulation (Park et al. 2019; Dubois et al. 2020), a cosmological zoom of the Horizon-AGN (Dubois et al. 2014) which will have tens of galaxies of a similar stellar mass to the one that we studied in this paper, along with several more massive objects. NEW-HORIZON also features AGN feedback and has reached  $z = 0.25$ , which also allows to comprehensively extend the redshift range of the analysis. Such a simulation will, thus, permit the extraction of a large sample of filaments from which to derive statistically meaningful quantities.

## ACKNOWLEDGEMENTS

We acknowledge useful discussions with Christophe Pichon and Harley Katz at various stages of this paper. This work used the DiRAC Data Centric system at Durham University, operated by the Institute for Computational Cosmology on behalf of the STFC DiRAC HPC Facility ([www.dirac.ac.uk](http://www.dirac.ac.uk)). This equipment was funded by a BIS National E-infrastructure capital grant ST/K00042X/1, STFC capital grant ST/K00087X/1, DiRAC Operations grant ST/K003267/1, and Durham University. DiRAC is part of the National E-Infrastructure. JD and AS are supported by Adrian Beecroft and the STFC, and CL by a Beecroft Fellowship. We warmly thank S. Rouberol for running the horizon cluster on which part of the simulation was post-processed. We thank D. Munro for freely distributing his YORICK programming language and OPENGL interface (available at <http://yorick.sourceforge.net/>).

## DATA AVAILABILITY STATEMENT

The data underlying this article will be shared on reasonable request to the corresponding author.

## REFERENCES

- Aragón-Calvo M. A., van de Weygaert R., Jones B. J. T., 2010, *MNRAS*, 408, 2163
- Aragón-Calvo M. A., van de Weygaert R., Jones B. J. T., van der Hulst J. M., 2007, *ApJ*, 655, L5
- Berlok T., Pfrommer C., 2019, *MNRAS*, 485, 908
- Bigiel F. et al., 2011, *ApJ*, 730, L13
- Birnboim Y., Dekel A., 2003, *MNRAS*, 345, 349
- Bond J. R., Kofman L., Pogosyan D., 1996, *Nature*, 380, 603
- Cadiou C., Dubois Y., Pichon C., 2019, *A&A*, 621, A96
- Cautun M., van de Weygaert R., Jones B. J. T., Frenk C. S., 2014, *MNRAS*, 441, 2923
- Chabrier G., 2003, *PASP*, 115, 763
- Chen Y.-C., Ho S., Blazek J., He S., Mandelbaum R., Melchior P., Singh S., 2019, *MNRAS*, 485, 2492
- Codis S., Pichon C., Devriendt J., Slyz A., Pogosyan D., Dubois Y., Sousbie T., 2012, *MNRAS*, 427, 3320
- Colberg J. M., Krughoff K. S., Connolly A. J., 2005, *MNRAS*, 359, 272
- Cornuault N., Lehnert M. D., Boulanger F., Guillard P., 2018, *A&A*, 610, A75
- Croton D. J. et al., 2006, *MNRAS*, 365, 11
- Danovich M., Dekel A., Hahn O., Teyssier R., 2012, *MNRAS*, 422, 1732
- Davis M., Huchra J., Latham D. W., Tonry J., 1982, *ApJ*, 253, 423
- Davé R., Anglés-Alcázar D., Narayanan D., Li Q., Rafieferantsoa M. H., Appleby S., 2019, *MNRAS*, 486, 2827
- Dekel A., Birnboim Y., 2006, *MNRAS*, 368, 2
- Dekel A. et al., 2009, *Nature*, 457, 451
- de Lapparent V., Geller M. J., Huchra J. P., 1986, *ApJ*, 302, L1
- Diemer B., Mansfield P., Kravtsov A. V., More S., 2017, *ApJ*, 843, 140
- Dijkstra E. W., 1959, *Numer. Math.*, 1, 269
- Dolag K., Meneghetti M., Moscardini L., Rasia E., Bonaldi A., 2006, *MNRAS*, 370, 656
- Dubois Y. et al., 2020, *A&A*, preprint ([arxiv:2009.10578](https://arxiv.org/abs/2009.10578))
- Dubois Y., Pichon C., Devriendt J., Silk J., Haehnelt M., Kimm T., Slyz A., 2013, *MNRAS*, 428, 2885
- Dubois Y., Teyssier R., 2008, *A&A*, 477, 79
- Dubois Y. et al., 2014, *MNRAS*, 444, 1453
- Dunkley J. et al., 2009, *ApJS*, 180, 306
- Elias L. M., Genel S., Sternberg A., Devriendt J., Slyz A., Visbal E., Bouché N., 2020, *MNRAS*, 494, 5439
- Freundlich J., Jog C. J., Combes F., 2014, *A&A*, 564, A7
- Gallego S. G. et al., 2018, *MNRAS*, 475, 3854
- Ganeshaiah Veena P., Cautun M., van de Weygaert R., Tempel E., Jones B. J. T., Rieder S., Frenk C. S., 2018, *MNRAS*, 481, 414
- Gao L., Theuns T., 2007, *Science*, 317, 1527
- Gardner J. P. et al., 2006, *Space Sci. Rev.*, 123, 485
- Geller M. J., Huchra J. P., 1989, *Science*, 246, 897
- Gheller C., Vazza F., Brüggén M., Alpaslan M., Holwerda B. W., Hopkins A. M., Liske J., 2016, *MNRAS*, 462, 448
- Gheller C., Vazza F., Favre J., Brüggén M., 2015, *MNRAS*, 453, 1164
- Giallisco M. et al., 2011, *ApJ*, 743, 95
- Grogin N. A. et al., 2011, *ApJS*, 197, 35
- Hartwig T., Bromm V., Loeb A., 2018, *MNRAS*, 479, 2202
- Ho S. H., Martin C. L., 2019, *ApJ*, 888, 11
- Japelj J. et al., 2019, *A&A*, 632, A94
- Jeans J. H., 1915, *MNRAS*, 76, 70
- Kacprzak G. G., Churchill C. W., Nielsen N. M., 2012, *ApJ*, 760, L7
- Katz H. et al., 2019, *MNRAS*, 494, 2200
- Katz N., 1992, *ApJ*, 391, 502
- Katz N., Keres D., Dave R., Weinberg D. H., Rosenberg J., Putman M., 2003, *Astrophys. Space Sci. Libr.*, 281, 185
- Kennicutt Robert C. J., 1998, *ApJ*, 498, 541
- Kereš D., Katz N., Weinberg D. H., Davé R., 2005, *MNRAS*, 363, 2
- Khandai N., Di Matteo T., Croft R., Wilkins S., Feng Y., Tucker E., DeGraf C., Liu M.-S., 2015, *MNRAS*, 450, 1349
- Kikuta S. et al., 2019, *PASJ*, 71, L2
- Kimm T., Cen R., Devriendt J., Dubois Y., Slyz A., 2015, *MNRAS*, 451, 2900
- Kimm T., Devriendt J., Slyz A., Pichon C., Kassian S. A., Dubois Y., 2011, *MNRAS*, preprint ([arXiv:1106.0538](https://arxiv.org/abs/1106.0538))
- Kimm T., Haehnelt M., Blaizot J., Katz H., Michel-Dansac L., Garel T., Rosdahl J., Teyssier R., 2018, *MNRAS*, 475, 4617
- Klar J. S., Mücke J. P., 2012, *MNRAS*, 423, 304



- Koekemoer A. M. et al., 2011, *ApJS*, 197, 36
- Kooistra R., Silva M. B., Zaroubi S., Verheijen M. A. W., Tempel E., Hess K. M., 2019, *MNRAS*, 490, 1415
- Kraljic K., Dave R., Pichon C., 2019, *MNRAS*, 493, 362
- Krolewski A., Ho S., Chen Y.-C., Chan P. F., Tenneti A., Bizyaev D., Kraljic K., 2019, *ApJ*, 876, 13
- Laigle C. et al., 2015, *MNRAS*, 446, 2744
- Latif M. A., Schleicher D. R. G., Spaans M., Zaroubi S., 2011, *MNRAS*, 413, L33
- Lee K.-G., Hennawi J. F., White M., Croft R. A. C., Ozbek M., 2014, *ApJ*, 788, 49
- Leroy A. K. et al., 2013, *AJ*, 146, 19
- Mandelker N., Nagai D., Aung H., Dekel A., Padnos D., Birnboim Y., 2019, *MNRAS*, 484, 1100
- Mandelker N., Padnos D., Dekel A., Birnboim Y., Burkert A., Krumholz M. R., Steinberg E., 2016, *MNRAS*, 463, 3921
- Mandelker N., van Dokkum P. G., Brodie J. P., van den Bosch F. C., Ceverino D., 2018, *ApJ*, 861, 148
- Martin D., Matuszewski M., Morrissey P., Neill J., Moore A., Steidel C., Trainor R., 2016, *ApJ*, 824, L5
- Mocz P. et al., 2019, *Phys. Rev. Lett.*, 123, 141301
- Muñoz-Cuartas J. C., Macciò A. V., Gottlöber S., Dutton A. A., 2011, *MNRAS*, 411, 584
- Nelson D. et al., 2018, *Comput. Astrophys. Cosmol.*, 6, 29
- Nelson D. et al., 2019, *MNRAS*, 490, 3234
- Ocvirk P., Pichon C., Teyssier R., 2008, *MNRAS*, 390, 1326
- Ocvirk P. et al., 2016, *MNRAS*, 463, 1462
- Ostriker J., 1964, *ApJ*, 140, 1056
- Padnos D., Mandelker N., Birnboim Y., Dekel A., Krumholz M. R., Steinberg E., 2018, *MNRAS*, 477, 3293
- Pandya V. et al., 2019, *MNRAS*, 488, 5580
- Park M.-J. et al., 2019, *ApJ*, 883, 17
- Pfommer C., Pakmor R., Schaal K., Simpson C. M., Springel V., 2017, *MNRAS*, 465, 4500
- Pichon C., Bernardeau F., 1999, *A&A*, 343, 663
- Pichon C., Pogosyan D., Kimm T., Slyz A., Devriendt J., Dubois Y., 2011, *MNRAS*, 418, 2493
- Pogosyan D., Bond J. R., Kofman L., Wadsley J., 1998, in Colombi S., Mellier Y., Raban B., eds, *Wide Field Surveys in Cosmology*, Frontières, Paris, p. 61
- Powell L. C., Slyz A., Devriendt J., 2011, *MNRAS*, 414, 3671
- Power C., Navarro J. F., Jenkins A., Frenk C. S., White S. D. M., Springel V., Stadel J., Quinn T., 2003, *MNRAS*, 338, 14
- Prescott M. K. M., Martin C. L., Dey A., 2015, *ApJ*, 799, 62
- Prunet S., Pichon C., Aubert D., Pogosyan D., Teyssier R., Gottloeber S., 2008, *ApJS*, 178, 179
- Rahman N. et al., 2012, *ApJ*, 745, 183
- Rasera Y., Teyssier R., 2006, *A&A*, 445, 1
- Ribaud J., Lehner N., Howk J. C., Werk J. K., Tripp T. M., Prochaska J. X., Meiring J. D., Tumlinson J., 2011, *ApJ*, 743, 207
- Rosdahl J., Blaizot J., 2012, *MNRAS*, 423, 344
- Rosen A., Bregman J. N., 1995, *ApJ*, 440, 634
- Schaap W. E., 2007, PhD thesis, Kapteyn Astron. Inst.
- Schaap W. E., van de Weygaert R., 2000, *A&A*, 363, L29
- Schaye J. et al., 2015, *MNRAS*, 446, 521
- Sousbie T., 2011, *MNRAS*, 414, 350
- Spitzer L., 1978, *Physical Processes in the Interstellar Medium*. Wiley, New York
- Stewart K. R., Brooks A. M., Bullock J. S., Maller A. H., Diemand J., Wadsley J., Moustakas L. A., 2013, *ApJ*, 769, 74
- Stewart K. R. et al., 2017, *ApJ*, 843, 47
- Stodólkiewicz J. S., 1963, *AcA*, 13, 30
- Sutherland R. S., Dopita M. A., 1993, *ApJS*, 88, 253
- Tempel E., Libeskind N. I., 2013, *ApJ*, 775, L42
- Teyssier R., 2002, *A&A*, 385, 337
- Tillson H., Devriendt J., Slyz A., Miller L., Pichon C., 2015, *MNRAS*, 449, 4363
- Umehata H. et al., 2019, *Science*, 366, 97
- van den Bergh S., 1962, *AJ*, 67, 486
- Vietri M., Ferrara A., Miniati F., 1997, *ApJ*, 483, 262
- Vogelsberger M. et al., 2014, *MNRAS*, 444, 1518
- Woods R. M., Wadsley J., Couchman H. M. P., Stinson H. M. P., Shen S., 2014, *MNRAS*, 442, 732
- Zabl J. et al., 2019, *MNRAS*, 485, 1961

## APPENDIX: DATA

In Table A1 (*no feedback* run) and Table A2 (*feedback* run), we present the redshift evolution of the filament radius, as fitted from the density, temperature, and vorticity field.

**Table A1.** Redshift evolution of the filament core radius derived from density ( $r_0$ ) and truncation radii derived from temperature ( $r_T$ ) and vorticity ( $r_\omega$ ) as fitted from the density, temperature, and vorticity fields extracted from the *no-feedback* run. See Section 3.2 for details.

$z$	DM			Gas		
	$r_0$ (kpc)	$r_T$ (kpc)	$r_\omega$ (kpc)	$r_0$ (kpc)	$r_T$ (kpc)	$r_\omega$ (kpc)
3.35	15.37 ± 6.66	32.94 ± 3.47	39.35 ± 8.38	9.29 ± 4.13	27.24 ± 6.07	23.02 ± 6.79
3.44	10.54 ± 4.48	31.56 ± 3.94	33.91 ± 4.23	9.82 ± 3.92	26.27 ± 6.21	25.01 ± 10.41
3.60	10.48 ± 4.22	33.82 ± 5.91	35.41 ± 6.45	7.66 ± 2.73	25.65 ± 5.04	17.65 ± 5.60
3.65	11.20 ± 3.62	33.62 ± 5.44	32.90 ± 5.04	7.34 ± 2.70	27.63 ± 6.28	18.68 ± 5.01
3.82	11.44 ± 4.59	28.83 ± 3.84	31.92 ± 4.66	6.18 ± 2.19	22.20 ± 6.36	16.29 ± 5.86
3.94	8.64 ± 3.89	27.12 ± 5.14	29.77 ± 6.11	4.27 ± 1.38	20.44 ± 4.52	14.95 ± 4.81
4.00	8.39 ± 3.82	28.57 ± 6.47	25.87 ± 4.48	5.04 ± 1.96	18.58 ± 3.96	21.70 ± 6.62
4.13	7.88 ± 3.64	26.57 ± 7.79	24.43 ± 5.05	3.96 ± 1.53	17.70 ± 4.12	14.48 ± 4.63
4.55	7.34 ± 3.50	20.28 ± 4.04	22.82 ± 5.57	4.45 ± 1.72	13.84 ± 2.64	13.33 ± 3.18
5.06	3.95 ± 2.27	17.14 ± 3.05	19.84 ± 3.55	3.68 ± 0.85	10.04 ± 2.34	10.13 ± 3.03
5.45	3.37 ± 1.53	14.75 ± 2.99	16.31 ± 3.37	2.96 ± 1.23	7.80 ± 2.13	6.89 ± 1.73
5.66	2.74 ± 1.74	11.27 ± 2.52	15.32 ± 4.32	2.99 ± 1.39	7.48 ± 2.22	.23 ± 1.45
7.00	1.75 ± 0.75	9.19 ± 2.58	10.33 ± 1.76	1.77 ± 0.79	3.79 ± 0.49	4.46 ± 0.66
8.09	1.59 ± 1.00	6.28 ± 1.48	8.18 ± 1.82	1.58 ± 0.74	3.78 ± 0.56	3.96 ± 0.58

**Table A2.** Redshift evolution of the filament core radius derived from density ( $r_0$ ) and truncation radii derived from temperature ( $r_T$ ) and vorticity ( $r_\omega$ ) as fitted from the density, temperature, and vorticity fields extracted from the *feedback* run. See Section 3.2 for details. Note the absence of data for the radii derived from vorticity and temperature, due to the destructive impact of feedback on these fields.

$z$	DM			Gas		
	$r_0$ (kpc)	$r_T$ (kpc)	$r_\omega$ (kpc)	$r_0$ (kpc)	$r_T$ (kpc)	$r_\omega$ (kpc)
3.26	10.31 $\pm$ 4.41	36.90 $\pm$ 5.36	35.11 $\pm$ 8.25	7.92 $\pm$ 3.77	–	–
3.35	10.96 $\pm$ 4.81	33.82 $\pm$ 6.43	33.82 $\pm$ 8.34	12.14 $\pm$ 7.02	–	–
3.44	10.71 $\pm$ 4.77	34.33 $\pm$ 5.42	34.05 $\pm$ 7.36	8.64 $\pm$ 3.95	–	–
3.53	16.01 $\pm$ 10.50	34.80 $\pm$ 12.75	38.96 $\pm$ 17.90	7.22 $\pm$ 4.23	–	–
3.60	11.20 $\pm$ 5.17	36.80 $\pm$ 12.47	35.69 $\pm$ 14.22	8.02 $\pm$ 7.38	–	–
3.65	11.86 $\pm$ 4.88	30.58 $\pm$ 3.67	31.68 $\pm$ 5.53	8.04 $\pm$ 3.75	–	–
3.82	10.45 $\pm$ 4.37	28.99 $\pm$ 3.93	30.51 $\pm$ 7.28	5.89 $\pm$ 2.79	–	–
3.96	10.28 $\pm$ 4.59	27.86 $\pm$ 4.01	24.48 $\pm$ 7.15	5.10 $\pm$ 2.29	–	–
4.00	7.33 $\pm$ 4.43	27.23 $\pm$ 4.84	22.41 $\pm$ 6.05	5.13 $\pm$ 2.28	–	–
4.02	9.36 $\pm$ 4.30	26.48 $\pm$ 4.34	24.21 $\pm$ 7.01	4.94 $\pm$ 2.34	–	–
4.56	8.61 $\pm$ 5.60	23.13 $\pm$ 4.57	23.13 $\pm$ 5.06	4.21 $\pm$ 2.10	–	–
5.45	3.37 $\pm$ 1.96	14.37 $\pm$ 3.83	12.99 $\pm$ 3.13	2.70 $\pm$ 1.55	–	–
5.67	2.13 $\pm$ 1.33	11.59 $\pm$ 2.57	11.66 $\pm$ 2.60	2.78 $\pm$ 1.50	–	–
6.99	1.80 $\pm$ 1.13	9.20 $\pm$ 2.69	9.20 $\pm$ 2.58	2.79 $\pm$ 1.51	–	–
8.09	1.58 $\pm$ 1.00	7.08 $\pm$ 2.19	6.30 $\pm$ 1.91	2.43 $\pm$ 1.49	–	–

**Table A3.** Redshift evolution of the model fitted density as extracted from the *no-feedback* run. See Section 3.2 for details.

$z$	DM			Gas		
	$\log_{10}(\rho_0/\text{gcm}^{-3})$	$\log_{10}(\rho_1/\text{gcm}^{-3})$	$r_1$ (kpc)	$\log_{10}(\rho_0/\text{gcm}^{-3})$	$\log_{10}(\rho_1/\text{gcm}^{-3})$	$r_1$ (kpc)
3.35	–26.08 $\pm$ 0.46	–26.50 $\pm$ 0.46	7.66 $\pm$ 3.15	–26.76 $\pm$ 0.34	–27.32 $\pm$ 0.36	12.36 $\pm$ 5.49
3.44	–26.12 $\pm$ 0.39	–26.63 $\pm$ 0.40	9.30 $\pm$ 3.62	–26.64 $\pm$ 0.64	–27.19 $\pm$ 1.01	16.32 $\pm$ 7.66
3.60	–26.05 $\pm$ 0.42	–26.43 $\pm$ 0.44	7.89 $\pm$ 3.20	–26.75 $\pm$ 1.15	–27.26 $\pm$ 0.38	8.69 $\pm$ 3.13
3.65	–26.03 $\pm$ 0.42	–26.56 $\pm$ 0.43	8.13 $\pm$ 3.00	–26.66 $\pm$ 0.38	–27.30 $\pm$ 0.38	7.82 $\pm$ 2.65
3.82	–26.04 $\pm$ 0.41	–26.37 $\pm$ 0.48	8.05 $\pm$ 3.00	–26.64 $\pm$ 0.41	–27.25 $\pm$ 0.37	8.82 $\pm$ 3.02
3.94	–25.85 $\pm$ 0.47	–26.50 $\pm$ 0.41	7.95 $\pm$ 3.42	–26.18 $\pm$ 0.64	–26.95 $\pm$ 1.19	7.68 $\pm$ 2.81
4.00	–25.83 $\pm$ 0.49	–26.45 $\pm$ 0.45	6.79 $\pm$ 2.80	–26.53 $\pm$ 0.45	–27.12 $\pm$ 0.39	7.70 $\pm$ 3.00
4.13	–25.80 $\pm$ 0.44	–26.52 $\pm$ 1.10	6.89 $\pm$ 2.75	–25.81 $\pm$ 1.85	–27.05 $\pm$ 0.37	6.76 $\pm$ 2.78
4.55	–25.81 $\pm$ 0.48	–26.34 $\pm$ 0.41	6.89 $\pm$ 2.97	–26.44 $\pm$ 0.45	–27.00 $\pm$ 0.36	7.17 $\pm$ 2.76
5.06	–25.58 $\pm$ 0.45	–26.43 $\pm$ 1.20	6.06 $\pm$ 2.80	–25.75 $\pm$ 2.00	–26.88 $\pm$ 0.36	6.27 $\pm$ 2.39
5.45	–25.66 $\pm$ 0.42	–26.06 $\pm$ 0.61	6.00 $\pm$ 2.55	–26.23 $\pm$ 0.42	–26.66 $\pm$ 1.30	5.92 $\pm$ 2.14
5.66	–25.62 $\pm$ 0.43	–26.41 $\pm$ 1.25	9.00 $\pm$ 4.78	–26.11 $\pm$ 0.56	–26.92 $\pm$ 0.44	5.47 $\pm$ 2.06
7.00	–25.42 $\pm$ 0.45	–26.20 $\pm$ 1.20	6.43 $\pm$ 4.50	–26.11 $\pm$ 0.53	–27.09 $\pm$ 0.07	6.39 $\pm$ 4.89
8.09	–25.32 $\pm$ 0.46	–25.97 $\pm$ 1.22	6.07 $\pm$ 3.69	–25.98 $\pm$ 0.57	–26.66 $\pm$ 0.36	4.53 $\pm$ 1.72

**Table A4.** Redshift evolution of the model fitted density as extracted from the *feedback* run. See Section 3.2 for details.

$z$	DM			Gas		
	$\log_{10}(\rho_0/\text{gcm}^{-3})$	$\log_{10}(\rho_1/\text{gcm}^{-3})$	$r_1$ (kpc)	$\log_{10}(\rho_0/\text{gcm}^{-3})$	$\log_{10}(\rho_1/\text{gcm}^{-3})$	$r_1$ (kpc)
3.26	–2.26 $\pm$ 0.46	–2.83 $\pm$ 0.41	8.45 $\pm$ 3.67	–26.85 $\pm$ 0.42	–27.18 $\pm$ 0.47	13.82 $\pm$ 6.81
3.35	–2.40 $\pm$ 0.46	–2.89 $\pm$ 0.46	9.08 $\pm$ 3.92	–26.98 $\pm$ 0.50	–27.32 $\pm$ 0.45	8.63 $\pm$ 3.50
3.44	–2.36 $\pm$ 0.42	–2.70 $\pm$ 0.44	8.38 $\pm$ 3.16	–26.81 $\pm$ 0.45	–27.17 $\pm$ 1.20	9.18 $\pm$ 3.34
3.53	–2.49 $\pm$ 0.59	–2.83 $\pm$ 0.51	8.16 $\pm$ 3.60	–26.94 $\pm$ 0.69	–27.26 $\pm$ 0.48	7.50 $\pm$ 2.78
3.60	–2.38 $\pm$ 0.56	–2.81 $\pm$ 0.53	5.86 $\pm$ 2.65	–26.62 $\pm$ 0.86	–27.08 $\pm$ 0.56	9.09 $\pm$ 3.67
3.65	–2.31 $\pm$ 0.43	–2.77 $\pm$ 0.55	8.80 $\pm$ 3.92	–26.79 $\pm$ 0.41	–27.33 $\pm$ 0.41	7.95 $\pm$ 3.16
3.82	–2.26 $\pm$ 0.42	–2.64 $\pm$ 0.62	7.69 $\pm$ 2.97	–26.69 $\pm$ 0.39	–27.18 $\pm$ 0.42	8.13 $\pm$ 3.18
3.96	–2.23 $\pm$ 0.41	–2.77 $\pm$ 0.42	9.47 $\pm$ 5.03	–26.64 $\pm$ 0.42	–27.02 $\pm$ 1.07	8.26 $\pm$ 2.98
4.00	–2.19 $\pm$ 0.44	–2.57 $\pm$ 0.62	7.69 $\pm$ 4.16	–26.64 $\pm$ 0.43	–27.13 $\pm$ 0.44	10.04 $\pm$ 6.40
4.02	–2.21 $\pm$ 0.41	–2.82 $\pm$ 1.03	7.88 $\pm$ 3.06	–26.61 $\pm$ 0.43	–26.97 $\pm$ 0.53	9.23 $\pm$ 3.70
4.56	–2.04 $\pm$ 0.44	–2.77 $\pm$ 1.17	6.59 $\pm$ 2.84	–26.52 $\pm$ 0.41	–27.00 $\pm$ 0.42	7.48 $\pm$ 2.75
5.45	–1.82 $\pm$ 0.40	–2.56 $\pm$ 1.17	6.53 $\pm$ 5.57	–26.27 $\pm$ 0.49	–26.95 $\pm$ 0.39	6.03 $\pm$ 2.49
5.67	–1.84 $\pm$ 0.44	–2.62 $\pm$ 1.30	5.77 $\pm$ 2.38	–26.35 $\pm$ 0.50	–26.92 $\pm$ 0.37	6.18 $\pm$ 2.40
6.99	–1.59 $\pm$ 0.49	–2.41 $\pm$ 1.23	3.74 $\pm$ 1.39	–26.15 $\pm$ 0.46	–26.81 $\pm$ 0.36	6.01 $\pm$ 2.38
8.09	–1.49 $\pm$ 0.57	–2.10 $\pm$ 0.42	3.36 $\pm$ 1.49	–26.03 $\pm$ 0.57	–26.88 $\pm$ 0.26	4.20 $\pm$ 1.66